Applied Thermal Engineering 177 (2020) 115493

Contents lists available at ScienceDirect

Applied Thermal Engineering

journal homepage: www.elsevier.com/locate/apthermeng

Phase change heat transfer in an L-shape heatsink occupied with paraffin-copper metal foam

Ali Chamkha[a,b], Ali Veismoradi[c], Mohammad Ghalambaz[d,e,*], Pouyan Talebizadehsardari[d,e,*]

[a] Institute of Research and Development, Duy Tan University, Da Nang 550000, Vietnam
[b] Institute of Theoretical and Applied Research (ITAR), Duy Tan University, Hanoi 100000, Vietnam
[c] Chemical Engineering Department, Ferdowsi University, Mashhad, Iran
[d] Metamaterials for Mechanical, Biomechanical and Multiphysical Applications Research Group, Ton Duc Thang University, Ho Chi Minh City, Vietnam
[e] Faculty of Applied Sciences, Ton Duc Thang University, Ho Chi Minh City, Vietnam

HIGHLIGHTS

- The melting/solidification in a metal foam L-shape heatsink is addressed.
- The heatsink is subject to a transient heat pulse.
- The enthalpy-porosity approach is utilized to model the phase change heat transfer.
- The finite element method with grid adaptation is used to solve the governing equations.
- The using the PCM-metal foam heatsink improves the transient heat transfer.

ARTICLE INFO

Keywords:
Heatsink
Thermal management
Metal foam
Phase change materials (PCMs)

ABSTRACT

The enormous transient heating loads can be occurred in various electronic components, and hence, the thermal management of such loads is a curial task. The current research aims to address the flow and heat transfer of Phase Change Materials (PCMs) embedded in metal-foams heatsink under pulse heating conditions. The heatsink is made of an L-shape enclosure with a mounted hot element at the vertical side. The element produces a pulse heat flux while the heatsink is cooled at its top wall by an external flow. As a result, the heatsink changes the direction of heat transfer by absorbing the heat from a vertical surface and dissipating through a horizontal surface. The governing equations for the phase change flow and heat transfer of PCM in a metal foam are present and transformed into a non-dimensional form to generalize the study. The finite element method with an automatic time-step and grid adaptation is adopted as the solution method. Due to the presence of unsteady heat flux, the PCM in the heatsink experiences both of the solidification and melting phase change phenome. The outcomes show that the PCM-heatsink enhances the cooling rate of the element on the activation of the heat pulse. The heatsink provides a uniform and constant efficiency during the pulse. The higher the pulse power, the higher the heatsink efficiency. The growth of the element heat flux to fourfold and sixfold of the steady heat flux results in a heatsink efficiency of $\eta = 1.75$ and $\eta = 2.4$, respectively.

1. Introduction

The phase change heat transfer has been investigated in various literature studies. Phase Change Materials (PCMs) are capable of storing/releasing a notable amount of thermal energy on phase change. The solid/liquid phase change has been extensively applied in various domestic and industrial applications such as buildings [1], solar energy [2], cold storage [3], microelectronics [4], and power generation [5].

The application of phase change materials can be divided into two categories of thermal energy storage and thermal management [1]. Although PCMs are capable of storing a tremendous amount of thermal energy in the form of latent heat, the poor thermal conductivity of these materials is an essential barrier to the practical application of PCMs. One of the applications of PCMs, which requires a high response time for thermal energy storage/release is a phase change heatsinks. A phase change heatsink can absorb thermal shocks of a thermal system by

* Corresponding authors at: Ton Duc Thang University, Ho Chi Minh City, Vietnam.
E-mail addresses: alichamkha@duytan.edu.vn (A. Chamkha), ali.veismoradi@mail.um.ac.ir (A. Veismoradi), mohammad.ghalambaz@tdtu.edu.vn (M. Ghalambaz), ptsardari@tdtu.edu.vn (P. Talebizadehsardari).

https://doi.org/10.1016/j.applthermaleng.2020.115493
Received 30 July 2019; Received in revised form 15 April 2020; Accepted 14 May 2020
Available online 21 May 2020
1359-4311/

Nomenclature

Latin symbols

A_{mush}	a big numeric value of order 10^6
Bi	Biot number, $h_\infty H/k_{m,l}$
C_p	the specific heat capacity (J/(kg.K))
Da	Darcy number, κ/H^2
e	a small numeric value of order 10^{-3}
g	the gravity constant (m/s^2)
H	cavity size – geometrical scale characteristics
h	the coefficient of external convective heat transfer (W/(m^2.K^1))
h_{sf}	the fusion latent heat (J/kg)
k	coefficient of thermal conductivity (W/(m.K)
MVF	the scaled molten volume
n	the surface normal vector (m)
p	the pressure (N/m^2)
P	the dimensionless pressure
Pr	Prandtl number, $\nu/\alpha_{m,l}$
$Q"$	the dimensionless wall heat flux
$q_0^{''}$	the wall heat flux (W/m^2)
Ra	Rayleigh number, $(g\beta_l \Delta T H^3)/(\nu_l \alpha_{m,l})$
s	the source term of the enthalpy-porosity in the momentum equation
S	the dimensionless source term
Ste	Stefan number, $((\rho C_p)_{m,l}\ \Delta T)/(\rho_l h_{sf,m})$
t	the dimensional time (s)
T	the temperature field (K)
u, v	the velocity in the × and y directions (m/s)
U, V	the dimensionless velocity in the X and Y -directions
x, y	the × and y -coordinates (m)
X, Y	the dimensionless X and Y –directions

Greek symbols

α	the coefficient of the thermal diffusivity (m^2/s)
β	the coefficient of volumetric thermal expansion (1/K)
δt	the heat pulse duration (s)
δT	the temperature bond of the phase change (K)
ΔT	the temperature scale (K), $q"_0 H/k_{m,l}$
$\delta\tau$	non-dimensional heat pulse duration
ε	porosity of the metal foam
η	heatsink efficiency
θ	non-dimensional temperature
κ	permeability of the metal foam (m^2)
λ	the intensity of the heating pulse power
μ	the dynamic viscosity (kg/(m.s))
ν	the kinematic viscosity (m^2/s)
ξ	the power of heat load, the basis function of the finite element method
ρ	density (kg/m^3)
τ	the non-dimensional time
ϕ	the melt volume fraction

Subscripts

0	start of heat pulse
1	end of heat pulse
∞	the external cooling flow
ave	average
b	bottom wall
f	fusion
l	liquid/molten PCM
m	effective of the PCM and porous matrix
s	solid PCM

storing/releasing exceed cooling/heat loads. However, damping of transient thermal loads demands a heatsink with a sufficiently high thermal response. Therefore, improving the thermal conductivity of PCMs materials and advancing the thermal design of phase change systems attracted the attention of many recent researchers [4,6,7]. Using nano additives and high-thermal conductive porous materials are two novel approaches to enhance the thermal conductivity of PCMs.

Regarding the phase change heat transfer of PCMs in clear flows (no porous medium), Bondareva and Sheremet [8] investigated the melting of a PCM in an enclosure. They showed that the natural convection heat transfer in liquid parts of the cavity plays an important role in the melting heat transfer. In another study, Bondareva and Sheremet [9] theoretically studied the natural convection melting of paraffin inside a rectangular enclosure heated by a conjugate element. Some researchers tried to use nanoparticle additives to enhance the thermal conductivity of PCMs and accelerate the phase change heat transfer. Kumar et al. [10,11] experimentally examined the melting of lead in a cavity while one side of the cavity [10], or both sides [11] were subject to a constant heat flux. Bertrand et al. [12] performed a benchmark study on the simulation of laminar melting and natural convection heat transfer in a cavity with a constant hot wall temperature. The outcomes reveal that the trends of most of the numerical approaches are in general agreement; however, there they are not coincident.

Bondareva et al. [13,14] explored the phase change melting heat transfer of n-Octadecane in an enclosure. The results show that the presence of nano additives improves the melting heat transfer in a conduction dominant melting regime. The influences of using hybrid nanoparticles [15,16], simple nanoparticles [17–19], hybrid nanoparticles and fins [20–22], and magnetic effects [23–26] on the phase change behavior of PCMs are investigated. The results show that the addition of nanoparticles can improve or deteriorate the phase change rate, depending on the geometrical aspects of the enclosure, type of the PCM, and type of nanoparticles. Moreover, generally, the magnetic field effect tends to suppress the natural convection in PCM-enclosures and mostly results in a reduction of the heat transfer rate.

Using high thermal conductive porous materials is another approach to enhance the heat transfer in enclosures. Considering natural convection heat transfer in enclosures with no phase change, Sivasankaran et al. [27] examined the natural convection heat transfer in a cavity filled with a porous medium. The results show that the increase of the metal foam porosity enhances the natural convection heat transfer. Ghalambaz et al. [28] investigated the conjugate natural convection heat transfer in a porous cavity for various locations of a hot and a cold element. The outcomes show that the location of the elements influences the natural convection heat transfer in the cavity, and there is an optimum location for the elements. Paknezad et al. [29] experimentally studied the effect of a metal foam porous medium on the free convection heat transfer in an aluminum-foam heatsink. The influence of the inclination angle of the heatsink on the thermal performance of the porous heatsink was analyzed. They reported that the maximum cooling efficiency is about %17, which occurs at an inclination angle of 90°. Moreover, considering heat transfer in porous media, various effects such as wall boundary conditions [30], double-diffusive [31], entropy generation [32], and cavity partially filled with porous medium [33–35] are investigated.

Literature review shows that the phase change heat transfer in porous media has been investigated only in a few studies. Xiao et al. [36] prepared samples of paraffin PCMs embedded in copper and nickel metal foams. The prepared samples of metal foams show high porosity above 90%. The thermophysical properties of the prepared samples

were measured and reported. It was found that using metal foams can notably enhance the effective thermal conductivity of the composite PCM-metal foam. The thermal conductivity of paraffin/nickel foam composite was increased about threefold compared to that of pure paraffin (PCM). Zheng et al. [37] experimentally addressed the effect of using copper metal foams for the phase-change heat transfer behavior of paraffin PCM. The results show that using copper metal foam can reduce the melting time up to 20.5%. Hossain et al. [38] simulated the free convection melting of PCMs in metal foams in a rectangular cavity enclosure. The top wall of the cavity was at a constant hot temperature while the other walls were perfectly insulated. The results show that an increase in the porosity of the metal foam decreases the melting rate. The study of Sivasankaran et al. [27] demonstrated that the heat transfer (with no phase change) is higher for a cavity with higher porosity. The difference between the outcomes of these two studies can be due to the heating boundary condition. In [27], the cavity was heated from the bottom, which induces a significant natural convection flow, but in [38], the cavity is heated from the top, which suppresses the natural convection flow and leads to a conduction dominant heat transfer regime.

Li et al. [39] explored the solidification of PCMs in a porous enclosure. Using a scale analysis technique, Jethelah et al. [40] addressed the natural convection heat transfer of PCMs in a cavity filled with a porous medium and heated from a sidewall. The results show that the increase of Rayleigh number or Darcy number enhances the melting rate. Ali et al. [41] employed the pin–fin configuration to improve the heat transfer capability of a paraffin wax filled heat sink. They found that there is an optimal diameter of pin-fins for the best heat transfer performance.

Considering PCMs in heatsinks for cooling of electronic components, Kandasamy et al. [42] investigated the thermal performance of using PCMs in the space between the fins of a horizontal heatsink. The results were promising for applications of PCM in the cooling of electronic components. Later, Zhu et al. [43] employed a layer of metal foam in the heatsink to further improve the heat transfer and investigated the aspect ratio of the metal foam layer to the clear flow layer. The results demonstrate that increasing the thinness of the metal foam layer always improves the heat transfer rate. However, filling the entire height of the heatsink with metal foam saturates the performance improvement.

In all of the above studies, the thermal load was steady, while there are practical situations in which the thermal load is unsteady. There are many reasons that the heat generation in electronic components could be periodic. An active electronic component usually produces a constant heating power, which is required for standby or typical functioning of the component. However, in some cases, such as load transients, switching conditions, temporary micro proceeding tasks, or temporally change of the operational conditions, the heating power of the components can sharply increase to a significantly high level. After the transient situation, the heating power can return to the normal level. Considering the pulse power, Alshaer et al. [44] experimentally investigated the thermal cooling of a heatsink filled with carbon foam–PCM–MWCNTs composite materials. The pulse power was made of a base heating power and an additional high power spike. The influence of various pulse modes was explored on the surface temperature of the heated surface. The results show that the presence of the PCM could effectively damp the transient temperatures and protect the electronic components. Ghalambaz and Zhang [45] theoretically investigated the conjugate phase change heat transfer of paraffin wax-Nickel foams in an annulus space for the transient cooling of batteries. They reported that the PCM-metal foams are beneficial for the transient heat dissipation. Hussain et al. [46] investigated lithium-ion batteries during the charging and discharging process and reported that the battery produces a transient heat load during each process. They utilized a phase change heatsink filled with paraffin-nickel foam as a thermal management system for cooling of the battery. The results show that utilizing the PCM can notably reduce the battery's surface temperature. Using paraffin-nickel foam can reduce the battery surface temperature by about 31% compared to natural air convection.

In all of the mentioned heatsink applications [41–46], the heatsink was placed horizontally over a horizontal heated surface [41–44], and it was insulated or cooled by its top horizontal surface, or the heating plate was inside the heatsink [45,46]. Thus, the heating surface and cooling surface were parallel. However, there are situations that the heated surface can be mounted vertically, and the cooling surface is at the top. For example, in the packaging of electronic devices, a CPU can be mounted vertically over a PCB board while the cooling flow is at the top of the package. In this situation, the alteration of the heat transfer path from the vertical heated surface to a horizontal cooling surface is demanded. The L-shape cavities are the best candidate for this task.

The literature review shows that the phase change heat transfer of PCM-metal foams subject to steady heat loads is theoretically investigated in some of the recent studies [38–40]. The phase-change processes involving a steady heat load are either subject to melting [38,40] or solidification [39]. However, the phase change heat transfer subject to a transient heat load experiences both of melting and solidification processes due to transient behavior of thermal load and external cooling power. Therefore, following the experimental studies of [46], the present study aims to address the phase change behavior of PCMs-metal foams in an enclosure subject to a heat pulse for the first time. Moreover, another contribution of the present work is the L-shape geometry of the heatsink, which connects the vertical heated surface to the horizontal cooling surface.

2. Mathematical model

2.1. Physical model

As shown in Fig. 1 (a), a heatsink is filled with copper metal foam with a porosity of ε and permeability of κ. The heatsink enclosure and the porous space is filled with paraffin wax PCM with the fusion temperature of T_f. The left wall of the heatsink is subject to a pulse heat flux with a steady power of $q“_0$, which raises to the value of $(1 + \gamma)\ q”_0$ during a time interval of δt, and then reduces to the steady heat flux of $q“_0$. The top of heatsink is subject to convective heat transfer cooling with a uniform temperature of T_∞, and a convective heat transfer coefficient of h_∞ where $T_\infty < T_f$. At rest, the PCM is at the initial uniform temperature of T_∞ then the heat flux elevates to the base power of $q”_0$ for a sufficiently long time until the heatsink reaches a steady-state situation. Then, suddenly the heat flux raises to the high heat flux of $(1 + \gamma)\ q“_0$ during t_0 to t_1 (a time interval of δt) commencing at t_0. At t_1, the heat flux reduces back to the steady heat flux $q”_0$. Here, γ indicates

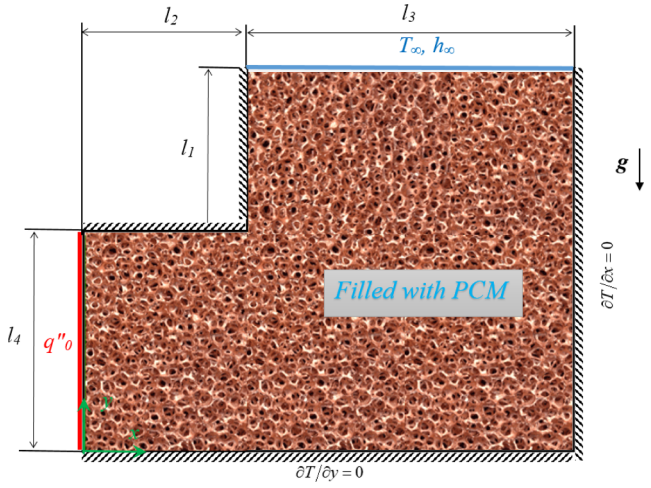

Fig. 1. Physical model of PCM-Metal foam heatsink.

the increase in the power of heat pulse with the relation of (1 + γ). For instance, γ = 1 shows that the heat flux has risen to two-fold, and γ = 2 indicates the raise of the surface heat flux by three-fold.

2.2. Governing equations

The set of governing equation for the phase change flow and heat transfer in the porous medium are as follows [45,47,48]:

$$\frac{\partial u}{\partial x}+\frac{\partial v}{\partial y}=0 \tag{1}$$

$$\frac{\rho_l}{\varepsilon}\frac{\partial u}{\partial t}+\frac{\rho_l}{\varepsilon^2}\left(u\frac{\partial u}{\partial x}+v\frac{\partial u}{\partial y}\right) =-\frac{\partial p}{\partial x}+\frac{\mu_l(T)}{\varepsilon}\left(\frac{\partial^2 u}{\partial x^2}+\frac{\partial^2 u}{\partial y^2}\right)-\frac{\mu_l(T)}{\kappa}u-s(T)u \tag{2}$$

$$\frac{\rho_l}{\varepsilon}\frac{\partial v}{\partial t}+\frac{\rho_l}{\varepsilon^2}\left(u\frac{\partial v}{\partial x}+v\frac{\partial v}{\partial y}\right) =-\frac{\partial p}{\partial y}+\frac{\mu_l}{\varepsilon}\left(\frac{\partial^2 v}{\partial x^2}+\frac{\partial^2 v}{\partial y^2}\right)-\frac{\mu_l}{\kappa}v-s(T)v+\rho_l g\beta_l(T-T_f) \tag{3}$$

Energy in metal foam:

$$(\rho C_p)_m\frac{\partial T}{\partial t}+(\rho C_p)_l\left(u\frac{\partial T}{\partial x}+v\frac{\partial T}{\partial y}\right)=k_m\left(\frac{\partial^2 T}{\partial x^2}+\frac{\partial^2 T}{\partial y^2}\right)-\varepsilon\rho_l h_{sf,l}\frac{\partial\phi(T)}{\partial t} \tag{4}$$

In the above equations, Here, κ and ε denote the permeability and porosity of the copper foam. Here, ρ, μ, β, C_p, k, and h_{sf} are the density, the dynamic viscosity, the specific heat capacity, the thermal conductivity, and the latent heat of fusion. As depicted in Fig. 1, g shows the gravitational constant. The subscripts of l, s, p, and m denote the liquid PCM, solid PCM, porous matrix and the effective properties, respectively.

In the above governing equations, the terms of $\frac{\mu_l(T)}{\kappa}u$ and $\frac{\mu_l(T)}{\kappa}v$ are the Darcy terms. The source term $\rho_l g\beta_l(T-T_f)$ denotes the buoyancy force. The source terms of $-s(T)u$ and $-s(T)v$ forces the flow velocity components to zero in solid regions. The terms s(T) depends on the melting fraction and will be introduced in the next equation. The term $\varepsilon\rho_l h_{sf,l}\frac{\partial\phi(T)}{\partial t}$ indicates the energy storage/release due to latent heat. The porosity (ε) in this term shows that only the PCM in the pores contributes to the phase change. The term ϕ is the molten volume fraction and is a function of temperature that will be introduced later.

The effective heat capacity $(\rho C_p)_m$ in the liquid and solid-state is evaluated as $(\rho C_p)_m=\phi(\rho C_p)_{m,l}+(1-\phi)(\rho C_p)_{m,s}$ where $\phi$is the molten volume fraction [47]. The effective heat capacity at the liquid and solid statuses are also evaluated as $\rho C_p)_{m,l}=\varepsilon(\rho C_p)_l+(1-\varepsilon)(\rho C_p)_l$ and $\rho C_p)_{m,s}=\varepsilon(\rho C_p)_l+(1-\varepsilon)(\rho C_p)_s$.

The effective thermal conductivity of the PCM-metal foam can be computed using available models in the literature [49] or directly from available experimental data. In the above governing equations, the source term $s(T)$ controls the momentum equation in solid and liquid regions. This term is in the form of Darcy term in a porous medium and sharply raises to a large value in a solid region, forcing the velocity components to zero. This term vanishes in the liquid region. The source term $s(T)$ is introduced as following [16]:

$$s(T)=A_{mush}\frac{(1-\phi(T))^2}{\phi(T)^3+e} \tag{5}$$

where A_{mush} is a large number of O(10^{+5}); e is a small number of O ($1\ 0^{-3}$), preventing a zero denominator. Here, $\phi(T)$ is the molten volume fraction which is a function of temperature as follow

$$\phi(T)=\begin{cases}0 & T<T_f-\frac{\delta T}{2}\\ \frac{T-T_f}{\delta T}+\frac{1}{2} & T_f-\frac{\delta T}{2}<T<T_f+\frac{\delta T}{2}\\ 1 & T>T_f+\frac{\delta T}{2}\end{cases} \tag{6}$$

In the above equation, it is assumed that the phase change occurs at the small temperature range of δT and the volume fraction changes linearly with the temperature. Outside the fusion temperature range, the PCM is in a fully solid ($\phi=0$) or fully liquid ($\phi=1$) state. The source term $\partial\phi/\partial t$ in the heat equation controls the energy storage/release during the phase change. This term is multiplied by the porosity of the metal foam (ε) as only the PCM in the pores contributes to the phase change, and the porous matrix does not undergo any phase change. Moreover, the viscosity is artificially assumed as a function of molten volume fraction as $\mu_l(\phi)=\mu_l+(1-\phi)$ [15]. In a liquid region where$\phi=1$, this term vanishes, and $\mu_l(\phi)$ reduces to the regular value of $\mu_l(\phi)=\mu_l$. In a solid region where$\phi=0$, this term reduces to a large value of $\mu_l(\phi)=\mu_l+1$, which helps the momentum equation to force the velocity components to zero in a solid region. Using artificial viscosity in the solid region and phase change interface helps the stability and the convergence of the solution.

Now, considering the physical model, depicted in Fig. 1, the associated boundary conditions are introduced as follows:

The right sidewall and a portion of the left side wall are adiabatic as

$$\frac{\partial T}{\partial n}=0 \tag{7a}$$

where n is the normal vector of the surface. The top wall is subject to convective heat transfer as

$$k_m\frac{\partial T}{\partial y}=h_\infty(T-T_\infty) \tag{7b}$$

A portion of the left wall is subject to a uniform time-dependent heat flux as

$$k_m\frac{\partial T(x,0)}{\partial y}=q_0^{''}(t) \tag{7c}$$

The walls and the melting front are considered as an impermeable, and the no-slip condition is employed for the fluid flow. A reference pressure point of zero pressure was also assumed at the bottom left corner of the metal foam. At the initial time, it is assumed that that the element is turned on with the steady power of $q_0^{''}$for a long time and the heatsink is steady-state. Then, the heat pulse occurs. So, the initial condition for the results with heat pulse is the steady-state solution at the regular power of the element, $q_0^{''}$.

It is appropriate to express Eqs. (1)–(10) into the non-dimensional forms using dimensionless variables as following

$$X=\frac{x}{H},\ Y=\frac{y}{H},\ U=\frac{uH}{\alpha_{m,l}},\ V=\frac{vH}{\alpha_{m,l}},\ \theta=\frac{T-T_\infty}{\Delta T},\ \tau=\frac{t\alpha_{m,l}}{H^2},\ S(\theta)=\frac{s(T)H^2}{\rho_l\alpha_{m,l}}$$
$$P=\frac{pH^2}{\rho\alpha_{m,l}{}^2},\ \alpha_{m,l}=\frac{k_{m,l}}{(\rho c_p)_{m,l}},\ \mathrm{Pr}=\frac{\nu}{\alpha_{m,l}},\ Ra=\frac{g\beta_l\Delta TH^3}{\nu_l\alpha_{m,l}},\ Ste=\frac{(\rho Cp)_{m,l}\Delta T}{\rho_l h_{sf}},\ Da=\frac{\kappa}{H^2} \tag{8}$$

where $H=l_1+l_4$ is the characteristic length, Ra is the Rayleigh number, and Pr is the Prandtl number. The temperature difference (ΔT) is introduced based on the temperature scaling defined as $\Delta T=q^{''}{}_oH/k_{m,l}$ where $k_{m,l}$ is the effective thermal conductivity of the liquid PCM saturated metal foam, and α is the thermal diffusivity. The geometrical non-dimensional parameters are $L_1=l_1/H$, $L_2=l_2/H$, $L_3=l_3/H=1$-L_2 and $L_4=l_4/H=1$-L_1.

Substituting Eq. (11) into Eqs. (1)–(10), the corresponding non-dimensional form of the governing Eqs. (12)–(23) is obtained as:

Momentum in x-direction:

$$\frac{1}{\varepsilon}\frac{\partial U}{\partial \tau}+\frac{1}{\varepsilon^2}\left(U\frac{\partial U}{\partial X}+V\frac{\partial U}{\partial Y}\right)=-\frac{\partial P}{\partial X}+A(\phi)\frac{\Pr}{\varepsilon}\left(\frac{\partial^2 U}{\partial X^2}+\frac{\partial^2 U}{\partial Y^2}\right)-\frac{\Pr}{Da}U-S(\theta)U \tag{9}$$

Momentum in y-direction:

$$\frac{1}{\varepsilon}\frac{\partial V}{\partial \tau}+\frac{1}{\varepsilon^2}\left(U\frac{\partial V}{\partial X}+V\frac{\partial V}{\partial Y}\right)=-\frac{\partial P}{\partial Y}+A(\phi)\frac{\Pr}{\varepsilon}\left(\frac{\partial^2 V}{\partial X^2}+\frac{\partial^2 V}{\partial Y^2}\right)-\frac{\Pr}{Da}V-S(\theta)V+\Pr Ra\theta \tag{10}$$

Energy in metal foam-PCM:

$$\left(\phi+(1-\phi)\frac{(\rho Cp)_{m,s}}{(\rho C_p)_{m,l}}\right)\frac{\partial \theta}{\partial \tau}+\left(\frac{(\rho C_p)_{m,l}}{(\rho C_p)_l}\right)^{-1}\left(U\frac{\partial \theta}{\partial X}+V\frac{\partial \theta}{\partial Y}\right)=\frac{k_m}{k_{m,l}}\left(\frac{\partial^2 \theta}{\partial X^2}+\frac{\partial^2 \theta}{\partial Y^2}\right)-\frac{1}{Ste}\frac{\partial \phi(\theta)}{\partial \tau} \tag{11}$$

where *Pr*, *Ra,* and *Ste* are the Prandtl number, Rayleigh number, and Stephan number, respectively. $A(\phi)$ is the non-dimensional function as $A(\phi) = 1+(1\text{-}\phi)/(\rho_l\alpha_{m,l})$, which artificially raises the viscosity to high values in the solid region.

The side walls and bottom are adiabatic as

$$\frac{\partial \theta}{\partial n}=0 \tag{12a}$$

The top wall is subject to convective heat transfer as

$$\left(\frac{k_m}{k_{m,l}}\right)\frac{\partial \theta}{\partial Y}=Bi\theta_\infty \tag{12b}$$

where $\mathrm{Bi} = h_\infty H/k_{m,l}$. The side wall is subject to a uniform heat flux as

$$\left(\frac{k_m}{k_{m,l}}\right)\frac{\partial \theta(X,0)}{\partial X}=Q'(\tau)\ \ and\ \ \ Q'(\tau)=\begin{cases}1+\gamma & \tau_0<\tau<\tau_1\\ 1 & \tau<\tau_0,\ \tau>\tau_1\end{cases} \tag{12c}$$

where $\tau_0 = t_0\alpha_{m,l}/H^2$, $\tau_1 = t_1\alpha_{m,l}/H^2$. The non-dimensional thermo-physical properties can be summarized as:

$$\frac{k_{m,s}}{k_{m,l}}\sim\frac{k_m}{k_{m,l}}\sim 1,\quad \frac{(\rho C_p)_{m,s}}{(\rho C_p)_{m,l}}=\frac{(1-\varepsilon)(\rho C_p)_p+\varepsilon(\rho C_p)_s}{(1-\varepsilon)(\rho C_p)_p+\varepsilon(\rho C_p)_l}\sim 1,\quad \frac{(\rho C_p)_{m,l}}{(\rho C_p)_l}=(1-\varepsilon)\frac{(\rho C_p)_p}{(\rho C_p)_l}+\varepsilon \tag{13}$$

$$\phi(\theta)=\begin{cases}0 & \theta\leqslant\theta_f-\frac{1}{2}\delta\theta\\ \frac{\theta-\theta_f}{\delta\theta}+\frac{1}{2} & \theta_f-\frac{1}{2}\delta\theta<\theta<\theta_f+\frac{1}{2}\delta\theta\\ 1 & \theta\geqslant\theta_f+\frac{1}{2}\delta\theta\end{cases} \tag{14}$$

where $\theta_f = (T_f - T_\infty)/\Delta T$.

The characteristic parameter of the present study is the dimensionless temperature of the vertical hated wall (θ_b) can be introduced as:

$$\theta_b=\frac{T_b-T_\infty}{\Delta T}\ \ at\ \ X=0 \tag{15a}$$

and accordingly, the average element temperature at the heated wall can be evaluated as:

$$\theta_{b,ave}=\frac{\int_0^{L_4}\theta_b}{L_4} \tag{15b}$$

In the case without heatsink, the energy balance at the element surface can be written as:

$$q''(t)\times l_4 = l_4\times h_\infty(T_b-T_\infty) \tag{16}$$

which can be written in a non-dimensional form as

$$\theta_{b,0}=\frac{Q'(\tau)}{Bi} \tag{17}$$

hence the heatsink efficiency is introduced as

$$\eta=\frac{Q'(\tau)}{Bi\theta_{b,ave}} \tag{18}$$

Finally, the melting volume fraction is evaluated as:

$$MVF=\frac{\int_A \varepsilon\phi dA}{\int_A \varepsilon dA} \tag{19}$$

As a case study, following the experimental study of Xiao et al. [36], the porosity value, ε is considered to be 0.975 (bulk value) for 5 PPI porous pores. The permeability is adopted from [50] as 2.7×10^{-7} m^2, and the effective thermal conductivity of metal foam-paraffin wax is adopted as $k_m = 4.8$ W/m.K from the experimental study of Xiao et al. [36]. The thermophysical properties of Paraffin (PCM) and copper (metal foam) are summarized in Table 1.

3. Numerical method

3.1. Mesh study

In most of the PCM studies, using Finite Volume Method (FVM) or FEM, the phase change bond is considered quite wide to avoid the convergence problems. Indeed, it should be noted that the convergence issue and expensive computations costs of the enthalpy-porosity models are not within the utilized FEM or FVM. The issue inherited from the modeling approach. The heat equation, Eq. (4), is a temperature base equation, while the phase change occurs at a constant temperature of T_f. Thus, if the phase change bond, δT in Eq. (6), approaches to zero, to simulate the fusion at an accurate temperature of T_f, then a discontinuity in Eq. (4) occurs where the temperature is constant, but there is heat transfer in the form of latent heat. In order to deal with this issue, the enthalpy-porosity models assume a phase change bond around the fusion temperature (δT) instead of a fixed fusion temperature. Thus, the phase change phenome takes place in a very narrow temperature range. Due to the presence of natural convection, the temperature gradients near to the phase change interface are high, which accordingly, the temperature variation at the melting front would be high. A high-temperature gradient at the phase change interface results in a narrow space for phase change. Indeed, the higher the temperature gradients at the melting front, the narrower physical space of the phase change. Therefore, an adequate mesh is also required to be able to capture the phase change in a tiny ribbon space in the domain of the solution. Moreover, on phase change, the velocity components change from the natural convection velocity in the liquid region to zero in the solid region. This change in the velocity component occurs in a narrow space in the domain of the solution. The energy storage/release takes place on the melting front and in the same narrow space. Therefore, the governing equations are highly non-linear and

Table 1
The thermo-physical properties of paraffin wax and copper foam [37].

Material	k (W/m.K)	ρ(kg/m^3)	h_{sf}(J/kg.K)	c_p (J/kg.K)	β(1/K)	μ(Pa.s)
Paraffin	0.3	900	148,800	2300	0.0005	0.00324
Copper foam	380	8900	–	386	–	–

unstable in such a melting/solidification phase change problems.

The most crucial issue with a small value δT is the region of phase change. In the case of $\delta T = 0$, the phase change occurs at a line. When δT is very small, the phase change occurs in a very narrow region. In this region, the latent heat transfer, change of thermophysical properties, and the change of velocities (form domain velocity in the liquid region to zero in the solid region) occur. Thus, for a case of small value δT, a very fine domain mesh is demanded, which consequently raises the computational costs.

A large value of δT helps with the convergence of equations, and the phase change region can be captured by using a moderated mesh. However, a wide phase change bond reduces the modeling accuracy and fails to capture the phase change at an adequate fusion temperature. Employing an adaptation technique helps to refine the mesh where it is needed, and hence, applying a small phase change bond (δT), and capturing the phase change region with a reasonable mesh size is possible. The adaptation technique can be employed in FVM as well. However, our codes were based on FEM, and hence, we implemented the adaptation technique in FEM.

In the present study, the finite element method with an automatic time-step and a grid adaptation scheme is utilized to handle the phase change heat transfer in the phase change heatsink. By introducing the following basis set $\{\gamma_k\}_{k=1}^{N}$, the pressure, the x-velocity, y-velocity, and the temperature are expanded, such as:

$$\begin{aligned} P &\approx \sum_{m=1}^{N} P_m \gamma_m(X,\ Y),\\ U &\approx \sum_{m=1}^{N} U_m \gamma_m(X,\ Y),\\ V &\approx \sum_{m=1}^{N} V_m \gamma_m(X,\ Y),\\ \theta &\approx \sum_{m=1}^{N} \theta_m \gamma_m(X,\ Y) \end{aligned} \tag{20}$$

Linear shape functions for the pressure and temperature are utilized. The employed set of the basis functions for the variables γ is the same, and the utilized grids are a triangle. By using the Galerkin finite element approach, the residual functions of the set of governing equations at each node of the internal domain are achieved as follows:

$$\begin{aligned} R_i^1 \approx{}& \frac{1}{\varepsilon}\sum_{m=1}^{N} U_m \int \frac{\partial \gamma_m}{\partial \tau}\gamma_i dXdY + \frac{1}{\varepsilon^2}\sum_{m=1}^{N} U_m \int \left[\left(\sum_{m=1}^{N} U_m\gamma_m\right)\frac{\partial \gamma_m}{\partial X} + \left(\sum_{k=1}^{N} V_m\gamma_m\right)\frac{\partial \gamma_m}{\partial Y}\right]\gamma_i dXdY\\ &+ \sum_{m=1}^{N}\int\left(-\sum_{m=1}^{N} P_m\gamma_m\right)\frac{\partial \gamma_m}{\partial X}\gamma_i dXdY + A(\phi)\frac{2Pr}{\varepsilon}\sum_{m=1}^{N} U_m \int \frac{\partial \gamma_m}{\partial X}\frac{\partial \gamma_i}{\partial X}dXdY\\ &+ A(\phi)\frac{Pr}{\varepsilon}\sum_{m=1}^{N} U_m \int\left[\frac{\partial \gamma_m}{\partial Y}\frac{\partial \gamma_i}{\partial Y}\right]dXdY + A(\phi)\frac{Pr}{\varepsilon}\sum_{m=1}^{N} V_m \int \frac{\partial \gamma_m}{\partial X}\frac{\partial \gamma_i}{\partial Y}dXdY\\ &- A(\phi)\frac{Pr}{Da}\int\left(\sum_{m=1}^{N} U_m\gamma_m\right)\gamma_i dXdY - S(\theta)\int\left(\sum_{m=1}^{N} U_m\gamma_m\right)\gamma_i dXdY \end{aligned} \tag{21a}$$

$$\begin{aligned} R_i^2 \approx{}& \frac{1}{\varepsilon}\sum_{m=1}^{N} V_m \int \frac{\partial \gamma_m}{\partial \tau}\gamma_i dXdY + \frac{1}{\varepsilon^2}\sum_{m=1}^{N} V_m \int \left[\left(\sum_{m=1}^{N} U_m\gamma_m\right)\frac{\partial \gamma_m}{\partial X} + \left(\sum_{k=1}^{N} V_m\gamma_m\right)\frac{\partial \gamma_m}{\partial Y}\right]\gamma_i dXdY\\ &+ \sum_{m=1}^{N}\int\left(-\sum_{m=1}^{N} P_m\gamma_m\right)\frac{\partial \gamma_i}{\partial Y}dXdY + A(\phi)\frac{2Pr}{\varepsilon}\sum_{m=1}^{N} V_m \int \frac{\partial \gamma_m}{\partial Y}\frac{\partial \gamma_i}{\partial Y}dXdY\\ &+ A(\phi)\frac{Pr}{\varepsilon}\sum_{m=1}^{N} U_m \int\left[\frac{\partial \gamma_m}{\partial Y}\frac{\partial \gamma_i}{\partial X}\right]dXdY + A(\phi)\frac{Pr}{\varepsilon}\sum_{m=1}^{N} V_m \int \frac{\partial \gamma_m}{\partial X}\frac{\partial \gamma_i}{\partial X}dXdY\\ &- A(\phi)\frac{Pr}{Da}\int\left(\sum_{m=1}^{N} V_m\gamma_m\right)\gamma_i dXdY - S(\theta)\int\left(\sum_{m=1}^{N} V_m\gamma_m\right)\gamma_i dXdY\\ &+ PrRa\int\left(\sum_{m=1}^{N} \theta_m\gamma_m\right)\gamma_i dXdY \end{aligned} \tag{21b}$$

$$R_i^3 \approx \sum_{m=1}^{N} U_m \int \frac{\partial \gamma_m}{\partial X}\gamma_i dXdY + \sum_{m=1}^{N} V_m \int \frac{\partial \gamma_m}{\partial Y}\gamma_i dXdY \tag{21c}$$

Table 2
The dependency of the $\theta_{b,\ ave}$ on the mesh size.

Case	Number of element	$\theta_{b,ave}$
Case I	867	0.9067
Case II	2503	0.9001
Case III	4427	0.8975
Case IV	6720	0.8981
Case V	9360	0.8981
Case VI	12,064	0.8979

$$\begin{aligned} R_i^4 \approx{}& \left(\phi + (1-\phi)\frac{(\rho Cp)_{m,s}}{(\rho C_p)_{m,l}}\right)\sum_{m=1}^{N}\theta_m \int \frac{\partial \gamma_m}{\partial \tau}\gamma_i dXdY\\ &+ \left(\frac{(\rho C_p)_{m,l}}{(\rho C_p)_l}\right)^{-1}\sum_{m=1}^{N}\theta_m \int\left[\left(\sum_{m=1}^{N} U_m\gamma_m\right)\frac{\partial \gamma_m}{\partial X} + \left(\sum_{m=1}^{N} V_m\gamma_m\right)\frac{\partial \gamma_m}{\partial Y}\right]\gamma_m dXdY\\ &+ \frac{k_m}{k_{m,l}}\sum_{m=1}^{N}\theta_k \int\left[\frac{\partial \gamma_m}{\partial X}\frac{\partial \gamma_i}{\partial X} + \frac{\partial \gamma_m}{\partial Y}\frac{\partial \gamma_i}{\partial Y}\right]dXdY - \frac{1}{Ste}\sum_{m=1}^{N}\frac{\partial \phi(\theta_m)}{\partial \theta}\int \frac{\partial \gamma_m}{\partial \tau}\gamma_i dXdY \end{aligned} \tag{21d}$$

where

$$\frac{\partial \phi(\theta)}{\partial \theta} = \begin{cases} 0 & \theta \leqslant \theta_f - \frac{1}{2}\delta\theta\\ \frac{1}{\delta\theta} & \theta_f - \frac{1}{2}\delta\theta < \theta < \theta_f + \frac{1}{2}\delta\theta\\ 0 & \theta \geqslant \theta_f + \frac{1}{2}\delta\theta \end{cases} \tag{22}$$

Gaussian quadrature with second-order accuracy is utilized to integrate the integrals in the residual equations. The grid adaptation is performed based on the melt volume fraction of ϕ_{adapt} but with a slightly broader temperature range to enclose the phase change space with a slightly wider domain. The following function was introduced as the adaptation area

$$\phi_{adapt}(\theta) = \begin{cases} 0 & \theta \leqslant \theta_f - \frac{3}{2}\delta\theta\\ 1 & \theta_f - \frac{3}{2}\delta\theta < \theta < \theta_f + \frac{3}{2}\delta\theta\\ 0 & \theta \geqslant \theta_f + \frac{3}{2}\delta\theta \end{cases} \tag{23}$$

where adaptation takes place at the space marked with $\phi_{adapt} = 1$. The area marked for adaptation covers an area around the melting front, which is slightly larger than the actual phase change space. A wider adaptation domain ensures a smooth transient grid size over the sensitive area and also provides the opportunity of skipping the adaptation procedure for some intermediate time-steps since the mesh adaptation is computationally an expensive step. As long as the melting front is in the adapted area, marked by $\phi_{adapt} = 1$, a new grid adaptation is not required. When the actual phase change domain (the domain with $0 < \phi < 1$) approaches to the boundaries of the adapted space, the domain marked with $\phi_{adapt} = 1$, a new mesh adaptation has to be performed. The mesh in the adapted area is fivefold finer than the mesh in the regular domain of the solution.

The selection of the time-step is also another crucial step, which was handled by a free-step automatic Backward Differentiation Formula (BDF). The free-steps are automatically selected within a BDF order in the range of one and two [51]. The Newton method is employed to iteratively solve the residual equations using A PARDISO solver [52–54] with a residual error of order 10^{-6}. The damping factor of the Newtonian method is fixed as 0.9. The grid check and validation are conducted in the following sub-sections after the estimation of non-dimensional parameters.

3.2. Non-dimensional parameters

A cavity of height $H = 10$ cm, occupied with 5 PPI copper foam ($\varepsilon = 0.975$) and filled with the paraffin wax, is considered as a case study. It is assumed that the cold wall at the top is subject to a uniform

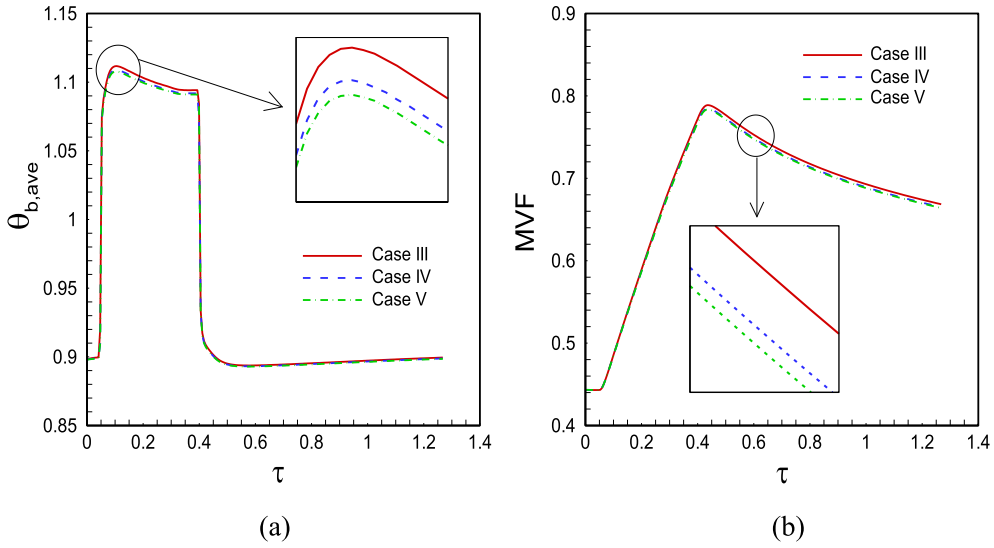

Fig. 2. The effect of mesh size on the characteristics results as a function of time; (a): Average temperature of hot element, $\theta_{b,\ ave}$; (b): The normalized melt volume fraction (*MVF*).

free stream temperature of $T_\infty = 14$ °C, and $h_\infty = 20$ W/m^{2}K. The fusion temperature is adopted as $T_f = 50$ °C. The permeability of the porous medium is 2.7×10^{-7} m^2 [50], and the effective thermal conductivity is $k_m = 4.8$ W/m.K [36]. The heat flux of the hot element is$q_0^{'} = 2500$ W/m^2. Other thermophysical properties are available in Table 1, and the effective thermal capacity is evaluated using the relations introduced in the text. It is assumed that $\gamma = 3$, and the pulse initiated at 100 s and continues to 1500 s, which as a result, the pulse duration is $\delta t = 1300$ s.

As in the definition of Stefan number can be seen, the Stefan number is a function of the ratio of the sensible heat and the latent heat, and the temperature scale (ΔT). In an experiment, in which the PCM material is fixed, the variation of the Stefan number can be controlled by controlling the imposed heat flux q_0. It is worth noticing that the aim of the current work is the investigation of the thermal response of the heatsink respect to the pulse heat flux. The pulse heat flux consists of a constant base heat flux q_0 and a transient pulse heat flux power $\gamma \times q_0$. In many of the literature-works, in which the thermal energy storage is the characteristic design goal, the Stefan number is the main control parameter. However, in the current study, the aim is the investigation of the heat transfer and cooling behavior of the heatsink. Thus, for a fixed PCM and porous matrix and under a fixed imposed heat flux (q_0), the Stefan number can be considered as a constant parameter. This is while the Rayleigh number is a function of various geometrical and external parameters, and it can notably influence the convection behavior of the molten region and heat transfer performance of the heatsink. Thus, the Rayleigh number and the magnitude of the pulse heat flux (γ) were selected as the controlling parameters.

The application of pulse heat can entirely depend on the electronic device. For example, harsh discharging of a battery pack may take about an hour where during this situation, the heat generation of the battery is high. The pulse loading of a hard-disk maybe only a few minutes to write backup data, and an image processing-CPU of a high-speed industrial camera may need only a few seconds to process an image. The pulse load of a CPU in a high-performance computer system could be a fraction of seconds in the interval of loading data from RAM and processing. In the present study, we selected the load conditions compatible with the capacity of the heatsink to demonstrate the capability of PCM-metal foam heatsinks in thermal management of transient load.

The non-dimensional parameters are also calculated as: $Ra = 3.023 \times 10^{+7}$, $Da = 2.7 \times 10^{-5}$, $Pr = 1.533$, $\varepsilon = 0.975$, $\theta_f = 0.691$, $(\rho C_p)_{m,s}/(\rho C_p)_{m,l} = 1$, $k_{m,s}/k_{m,l} = 1$, $\gamma = 3$, $\tau_1 = 0.047$, and $\delta\tau = 0.305$. The geometrical parameters are kept fixed as $L_1 = 0.5$, and $L_2 = 0.3$. These non-dimensional parameters are adopted for the computations; otherwise, it will be stated. The range of investigated parameters is as follows $0 < \gamma < 5$,$0.25 < \theta_f < 2.5$, $2 < Bi < 17$, and $5 \times 10^6 < Ra < 7 \times 10^7$. This range was selected based on the geometrical size of the heatsink and thermophysical parameters, as discussed in this section.

3.3. Mesh check

In order to ensure the accuracy of the results and quality of the utilized mesh, a mesh study is performed for the default case of the non-dimensional parameters, discussed in the sub-section 3.2. Six different meshes sizes are utilized, which the number of the elements for each utilized mesh is reported in Table 2 for a steady-state case. The number of elements in Table 2 is corresponding to an initial mesh with no adaptation. The average value of the hot-element temperature ($\theta_{b,ave}$) for each case is reported in Table 1. in a table (steady-state). The results for $\theta_{b,ave}$ and *MVF* as a function of τ for the default case of pulse heating ($\gamma = 3$) are plotted in Fig. 2(a) and (b), respectively. In these figures, the results are plotted for the meshes of III, IV, and V solely to avoiding the congestion of the curves. As seen in these figures and Table 2, the results of case III, are in agreement with the results of Case IV and V. The results for the two cases of IV and V are almost equivalent; however, the computational cost of Case V is much higher than those of Cases III and IV. Therefore, as a trade between the computational cost and accuracy, Case IV is selected for the computations of the current research.

Fig. 3 depicts the grid adaptation during the melting process at various stages of the solution. Fig. 3(a) shows the utilized mesh at the initial state of the solution with no adaptation. As seen, the mesh is denser near the walls. A denser mesh near the walls is required to capture the velocity and temperature gradients in these areas. In contrast, Fig. 3 (b) and (c) depicts the mesh at two non-dimensional times of $\tau = 0.2$ and $\tau = 0.4$. The mesh adaptation occurs around the melting front to enclose the phase change region with a much finer mesh. As discussed in the numerical method, the mesh in the adapted area is fivefold finer than the regular areas. A comparison between Fig. 3(b) and 3(c), shows that the mesh adaptation follows the melting front by advancing of the melting process in a direction away from the hot element.

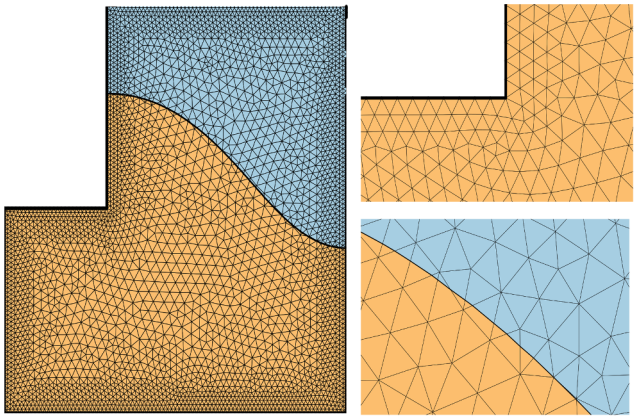

(a): Steady state

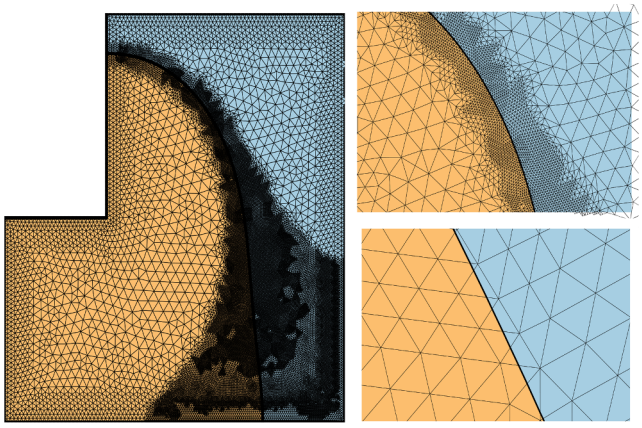

(b): τ = 0.2

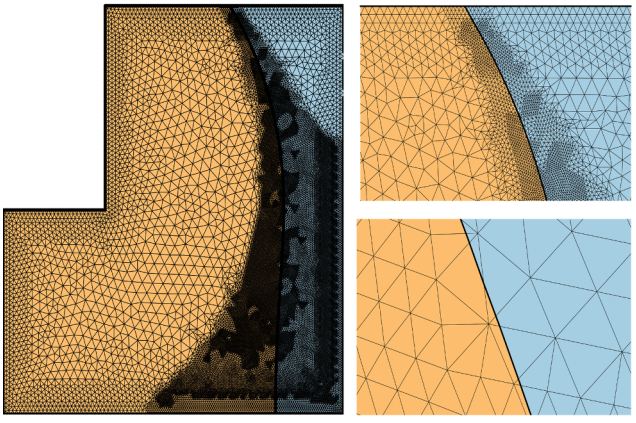

(c): τ = 0.4

Fig. 3. The initial mesh and adapted mesh of Case IV during the melting process.

3.4. Validation

The accuracy and correctness of the computations and the introduced model of phase change are evaluated through a comparison of the results with the theoretical and experimental results available in the literature. As a first case, the results of the current work are compared with the benchmark results of Bertrand et al. [12] for the melting of octadecane in a square cavity with no porous medium (Fig. 4). In this case, it is assumed that $\varepsilon = 1$, and $Da \rightarrow \infty$, The left wall is at an isothermal temperature, and the other walls are well insulated. The

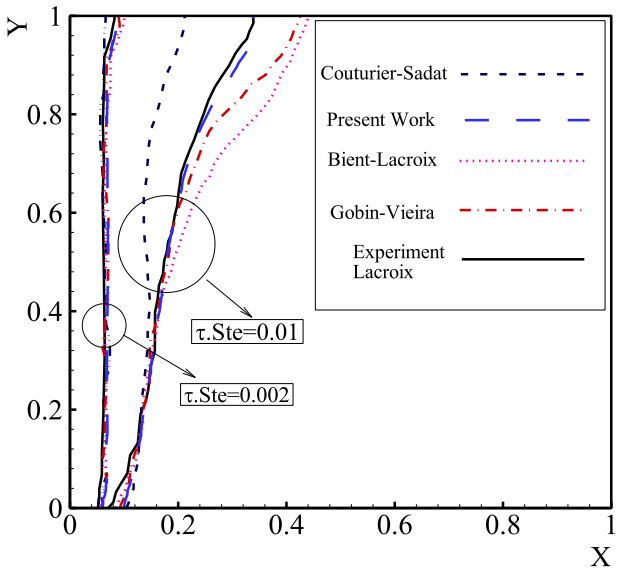

Fig. 4. A comparison between the results of the present study and literature review of Bertrand et al. [12].

Table 3
A comparison between the location of the melting front obtained in the present study and those reported in [10] for X location of the melting front against Y.

Y	τ = 1.1		τ = 1.47	
	Present work	Kumar et al. [10]	Present work	Kumar et al. [10]
0	0.17	0.12	0.22	0.21
0.1	0.19	0.15	0.26	0.23
0.2	0.21	0.18	0.33	0.26
0.3	0.28	0.23	0.39	0.27
0.4	0.30	0.24	0.43	0.35
0.5	0.30	0.29	0.59	0.56
0.6	0.41	0.37	0.71	0.66
0.7	0.52	0.53	0.80	0.77
0.8	0.58	0.57	0.82	0.82
0.9	0.57	0.58	0.82	0.83
1	0.59	0.57	0.85	0.85

comparison is performed for the case of octadecane when $Pr = 50$, $Ra = 10^{+7}$, and $Ste = 0.1$. The melting front at two time-steps of $\tau = 0.002$ and 0.01 are reported. As seen, the trend of the numerical results are in agreement, and the numerical results of the present work are in agreement with the experimental results.

As the second comparison, the results of the present study are compared with the results of the experimental study of Kumar et al. [10] for the melting of lead in a cavity. The experimental study performed for the melting of the lead subject to a constant heat flux at the right wall of the cavity while the other walls were insulated. The melting images of Kumar et al. [10] are obtained by thermal neutron radiography. The comparison is performed for a case with $Ste = 0.4$, $Pr = 0.0236$, $Ra = 1.4 \times 10^{+7}$, (heater input 16.3 kW/m^2, temperature at left side 555 K and temperature at the element side 599 K). The location of the melting front reported in [10] and computed in the present study are compared in Table 3.

Considering a case with no phase change, for Darcy natural convection heat transfer in a square cavity with temperature difference at the sidewalls and insulation at the top and bottom walls, the average Nusselt number for the case of $Ra \times Da = 100$ is obtained as 3.11. The average Nusselt number in the study of Sheremet and Pop [30], and Beckermann et al. [55] was reported as 3.10 and 3.11, respectively, which are almost the same as the present results.

Finally, the experimental study of Zheng et al. [37] for the melting of paraffin-copper foam in a cavity is adopted for comparison, and the

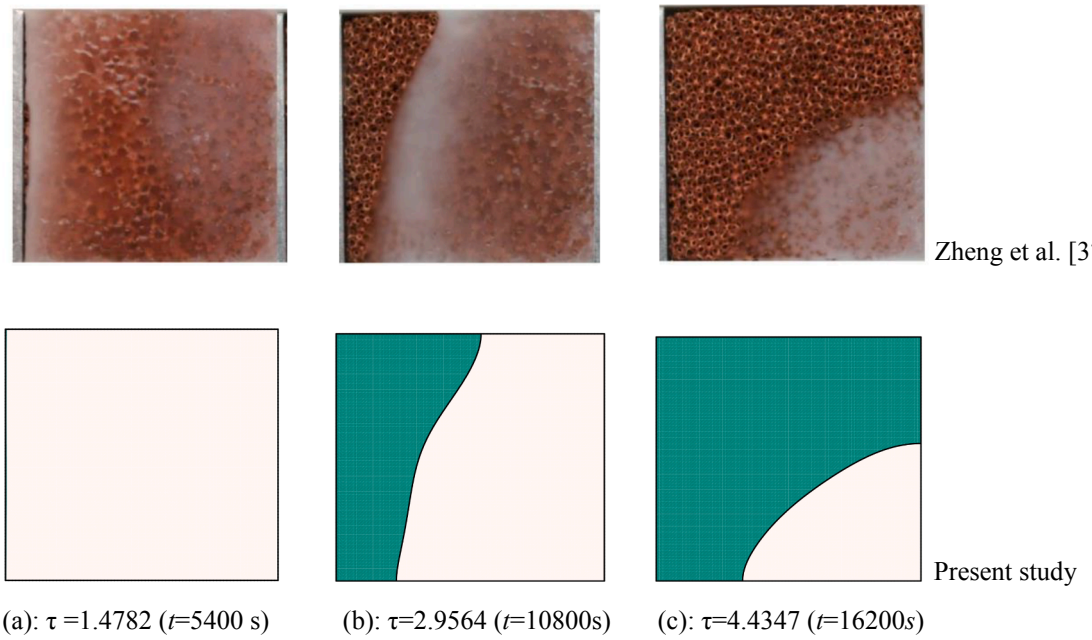

Fig. 5. The result of the melting of paraffin in copper metal foam, and a comparison of the numerical results of the present study with the experimental results of Zheng et al. [37].

results are plotted in Fig. 5. In [37], the porosity of the copper metal foam was $\varepsilon = 0.95$ with a pore size of 5PPI. The thermophysical properties for paraffin wax and the porous matrix are adopted from Table 1, and the effective specific heat capacity ratio is evaluated using the relations discussed in the text. The effective thermal conductivity adopted from the experimental study of Xiao et al. (2013) as $k_{eff} = 5$ W/m.K, the element power at the hot wall was$q_0^{'} = 1150$ W, and $H = 0.1$ m.

4. Results and discussions

The heat transfer behavior of the phase change heatsink is studied for two cases of steady-state (case $\gamma = 0$) and unsteady heat transfer subject to a heat pulse. In the steady-state heat transfer, there is a balance between the power of the heat pulse and the cooling power heat transfer to the external cold stream. In this case, the heatsink can be in a solid, liquid, or solid/liquid state, depending on the external cooling power. In the unsteady case, which the heat pulse is active, the presence of an active heat pulse increases the heat flux magnitude of the element, and hence, a transient heat transfer behavior occurs. The default-set of the non-dimensional parameters, as introduced before, is adopted for both steady and unsteady cases; otherwise, the value of the non-dimensional parameter will be stated. In all of the contour images, the difference between the contour levels is 0.1.

4.1. The steady-state heat operation of heatsink when $\gamma = 0$

Fig. 6 depicts steady-state temperature contours and streamlines in the heatsink for various values of the Rayleigh number. In Fig. 6, the streamlines are plotted in the molten PCM, and there is no streamline in the solidus PCM. The magnitude of normal melt volume fraction (*MVF*) and the average temperature of the element is also reported below each contour. Fig. 8 shows that the increase of Rayleigh number pushes the molten area toward the cold surface. When the Rayleigh number is comparatively low, the increment of the Rayleigh number induces a significant effect on the circulation flows (streamlines) and the temperature distribution. As the Rayleigh number grows, its effect on the isotherms and streamlines reduces. This is because of the constant power of the element. The generated heat of the element first reaches the molten region and then moves into the solid region. Then, the heat reaches the external cold stream and will be extracted from the heatsink. In the steady-state, there is a balance between the thermal resistance of each region and the temperature difference between the element temperature and the external temperature of θ_∞. The increase of the Rayleigh number decreases the thermal resistance in the molten region. Therefore, as can be seen in Fig. 6, the average temperature of the element reduces by the raise of the Rayleigh number. However, the rise of Ra only slightly reduces *MVF*, and it only smoothly affects the shape of the molten region.

Indeed, when the Rayleigh number is high, the thermal resistance of the molten region is much lower than the thermal resistance of the solid region due to the presence of significant natural convection circulation. Therefore, a further increase of Rayleigh number only slightly contributes to the molten region and *MVF*. According to Fig. 6, the dimensionless average temperature of the bottom wall (hot element) reduces from 1.05 to 0.85 by the increase of Rayleigh number from 6.16×10^6 to 6.16×10^7. Furthermore, the streamlines tend to be denser with an increment of *Ra* denoting higher velocity magnitudes in the molten region.

Rayleigh number can be used as a criterion for assessing the melting front's position, which specifies the boundary between liquid and solid regions. The melt volume fraction of$\phi = 0.5$ is adopted as the melting front. The melting front is plotted in Fig. 7 for various values of Rayleigh number. Fig. 7 shows with decreasing Ra number, the melting front is placed far away from the wall where the heat source is located. The increase of Rayleigh number slightly affects the top areas of the melting front as they are close to the cold surface with high cooling power. The increase of Rayleigh number mostly affects the bottom areas of the melting front by shifting the melting front toward the hot element and causing the reduction of *MVF*. The shift of the melting front toward the hot element is due to the reduction of the element temperature ($\theta_{b,ave}$). As it was discussed in the description of Fig. 6, the reduction of element temperature by the increase of Rayleigh number was due to the reduction of thermal resistance in the molten region.

Fig. 8 illustrates the local temperature of the element. The temperature rises gradually by moving along the element from the bottom toward the top of the element. There is a natural convection flow of liquid PCM in the molten region of the cavity. The fresh cold liquid first

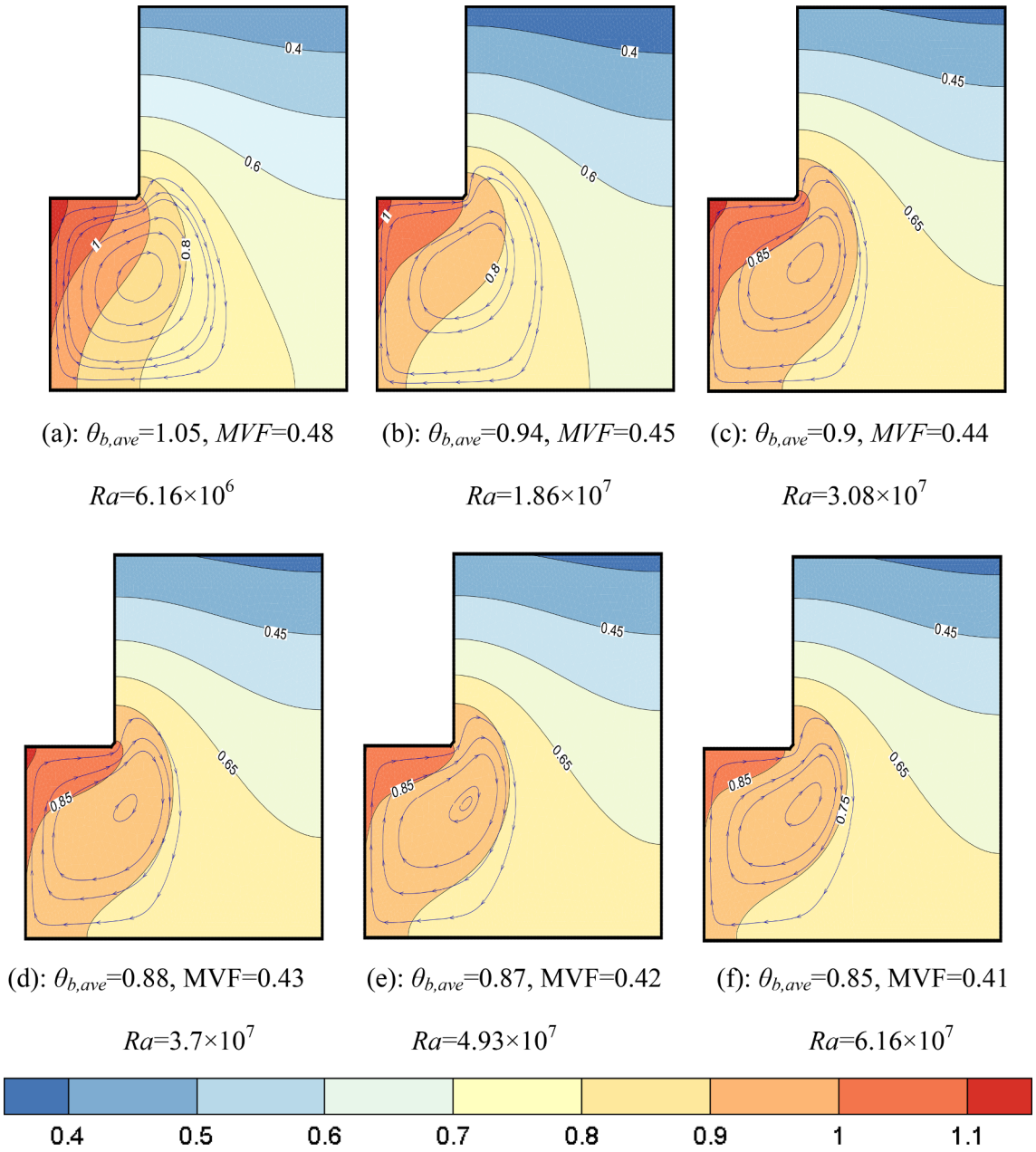

Fig. 6. Temperature contours and streamlines (in the same figure) for the default case, and different values of *Ra* number.

reaches the bottom of the element. The cold liquid over the element absorbs heat and gets warm. A warm liquid is lighter with a tendency to move upward with the natural convection potential to continue a flow circulation in the cavity. Then, the hot liquid reaches the melting front and gets cold. The cold liquid moves downward until it reaches the bottom of the element. Therefore, the bottom of the hot element, which is subject to the fresh cold liquid is cooler than the top of the element, and accordingly, the temperature from bottom to top rises gradually. According to Fig. 8, the dimensionless temperature decreases with the growing of the *Ra* number in any given location. This is due to the reduction of thermal resistance in the molten region by the increase of Rayleigh number.

Fig. 9 (a) shows the dimensionless trend of the average temperature of the hot element against Rayleigh number and several values of the Biot number (external cooling power). When the *Ra* increases, the values of $\theta_{b,ave}$ decreases nonlinearly. However, *Bi* number is another factor that can influence on $\theta_{b,ave}$. Fig. 9 (a) illustrates that the dimensionless wall temperature reduces about $\Delta\,\theta_{b,ave} = 0.33$ by the raise of *Bi*. However, the influence of the Biot number on the element temperature reduces by the increase of the Rayleigh number. The temperature of the wall decreases to a specific value, which is around 0.72, and then, it tends to remain constant. Attention to set of the non-dimensional parameters shows that the non-dimensional fusion temperature is $\theta_f = 0.691$. Therefore, it can be concluded that the increase of Rayleigh number and Biot number tend to reduce the wall temperature to a temperature about the fusion temperature. Any increase of wall temperature beyond the fusion temperature demands a solid-state in the entire cavity, which suppresses the natural convection effects and increases the overall thermal resistance of the heatsink.

Fig. 9 (b) displays the influence of the dimensionless fusion temperature on the element temperature, $\theta_{b,\,ave}$. This figure, in agreement with previous figures, shows that the raise of Rayleigh number reduces the element temperature smoothly. However, the variation of fusion temperature significantly changes the element temperature. The growth of the fusion temperature reduces the impact of circulation flows (Rayleigh number) on the element temperature. When the fusion

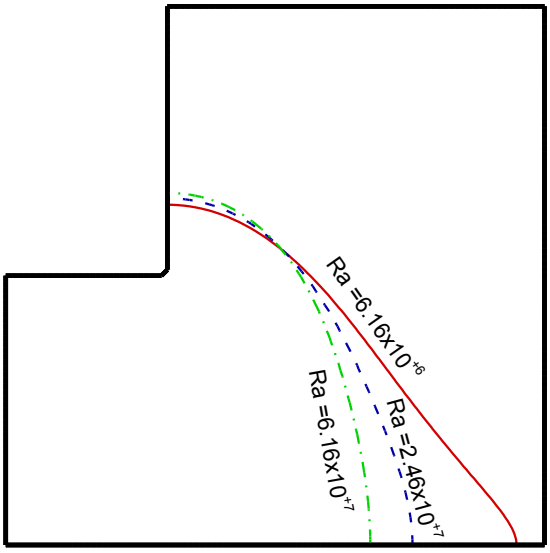

Fig. 7. Displacement of melting front ($\phi = 0.5$) for various values of *Ra*.

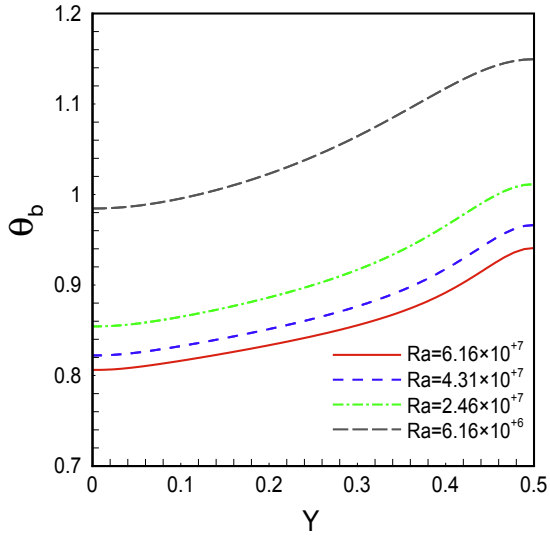

Fig. 8. Local temperature of the heated wall at different Rayleigh numbers.

temperature rises to $\theta_f = 2.17$, the effect of variation of Rayleigh on the wall temperature is not notable.

Indeed, the increase of non-dimensional fusion temperature develops the regions occupied by the solid PCM and shrinks the molten region. In the case of $\theta_f = 2.17$, the entire cavity is in solid-state, and there is no liquid region to be affected by the variation of Rayleigh number. In the case of $\theta_f = 0.25$, a large area of the cavity is molten, and an increase of the Rayleigh number tends to boost the natural convection flow and reduce the element temperature. Moreover, the increase in the fusion temperature increases the element temperature.

As mentioned, when the fusion temperature increases, the portion of the solid region in the cavity increases. Due to the absence of natural convection in the solid region, the thermal resistance of a solid region is notably higher than that of a molten region associated with a natural convection flow. Therefore, any development of solid PCM regions raises the element temperature.

4.2. The unsteady heat transfer due to a heat pulse

Fig. 10 shows a comparison between isotherms and streamlines for three pulse powers of $\gamma = 1, 3, 5$ and for various dimensionless time steps. As seen, at the initial stages, the isotherms and the streamlines have remained constant when γ increments at $\tau = 0.012$ since the heat pulse are actuated at $\tau = 0.047$. Indeed, Fig. 10 (a)-(c) depict the initial solution before the actuation of the heat pulse.

Fig. 10 (d), (e) and (f) depict the isotherms and streamlines at three pulse powers of $\gamma = 1, 3, 5$ when $\tau = 0.35$. The heat pulse turns off at $\tau = 0.35$. Therefore, these figures represent the results just when the heat pulse turns off. Fig. 10 (f) shows that the molten region in the case of high pulse power ($\gamma = 5$) is almost occupied the entire of the heatsink. In these figures, the contour level of $\theta = 0.7$ is about the fusion temperature and roughly can be considered as the melting front. In the case of $\gamma = 1$, only a small portion of the cavity is in a molten state, and the molten area grows by boosting the pulse power. Attention to Fig. 10 (f) shows that the streamlines are well distributed as the molten region is completely developed in the cavity in the case of $\gamma = 5$. In the case of low pulse power, *i.e.,* $\gamma = 1$, the solid region is almost covered half of the heatsink space, and a significant temperature gradient can be observed in the solid region. This is due to the low conduction dominant effect in the solid region. By the increase of pulse power, the temperature rises at the element location. The increase of pulse power also intensifies the temperature gradients at the element surface. This increase of temperature gradients is in agreement with the imposed boundary condition of Eq. (10) (c).

Fig. 10 (g), (h) and (i) display the isotherms and streamlines at $\tau = 0.4$. This is a short time after the heat pulse turns of and the heat flux reduces to the steady pulse power. Considering case $\gamma = 1$, a comparison between the results of Fig. 10 (d) and (g) show that both figures are very similar. Indeed, although the transient heat pulse is turned off, its effect has not been propagated in the liquid region. The same conclusion is true for the case of $\gamma = 3$. However, a comparison between Fig. 10 (f) and (i) reveals that the heat is still propagating in the liquid region toward the top regions of the heatsink during a short time after transient heat pulse since the liquid is still hot.

Fig. 10 (j), (k) and (l) are plotted for $\tau = 0.47$. The heat pulse duration was 0.0.305, and it was deactivated at $\tau = 0.35$, and hence, the time step of $\tau = 0.47$ displays the results at $\Delta\tau = 0.12$ after the pulse power turned off. This time is about 42% of the duration of the heat pulse. A comparison with previous time-steps reveals that in the case of low pulse power ($\gamma = 1$), the melting process has stopped in most areas of the heatsink, and the external cooling flow tends to reduce the temperature of the solid region at the top of the heatsink. Solely at the bottom of the heatsink, slight degrees of the melting front advancement can be observed, *i.e.*, the level of $\theta = 0.7$ has slightly shifted away from the element. In the case of moderate pulse power of $\gamma = 3$, a reshaping of the melted area can be observed. The overall melted and solid regions are the same as the previous step of $\tau = 0.4$; however, a thin layer of solid is formed over the cold wall. A comparison between the isotherms of steady-state results of Fig. 10 (a), (g), and (j) reveals that the natural convection flow and temperature distributions in the molten area of the heatsink are close to their steady-state situation.

Comparison between Fig. 10 (h) and (k) interestingly reveals that melting advanced at the bottom of the heatsink, and simultaneously, the solidification occurred at the top of the cavity. The hot liquid in the molten region has melted the solid PCM at the bottom of the heatsink. The bottom of the heatsink is an area which is connected to the adiabatic walls and does not have a cooling or heating support. The top area of the heatsink is connected to the cold wall with external cooling support. Hence, the bottom area is melting while the top region is freezing due to the external cooling power. This behavior is mainly due to the presence of the metal foam, which enhanced the thermal conductivity of the PCM. An enhanced thermal conductivity facilitates the thermal diffusivity, and hence, the thermal effect of the heatsink boundaries can further advance in the heatsink.

The trend of results for the case of $\gamma = 5$ is almost the same. The solidification started at the top of the cavity. However, the amount of

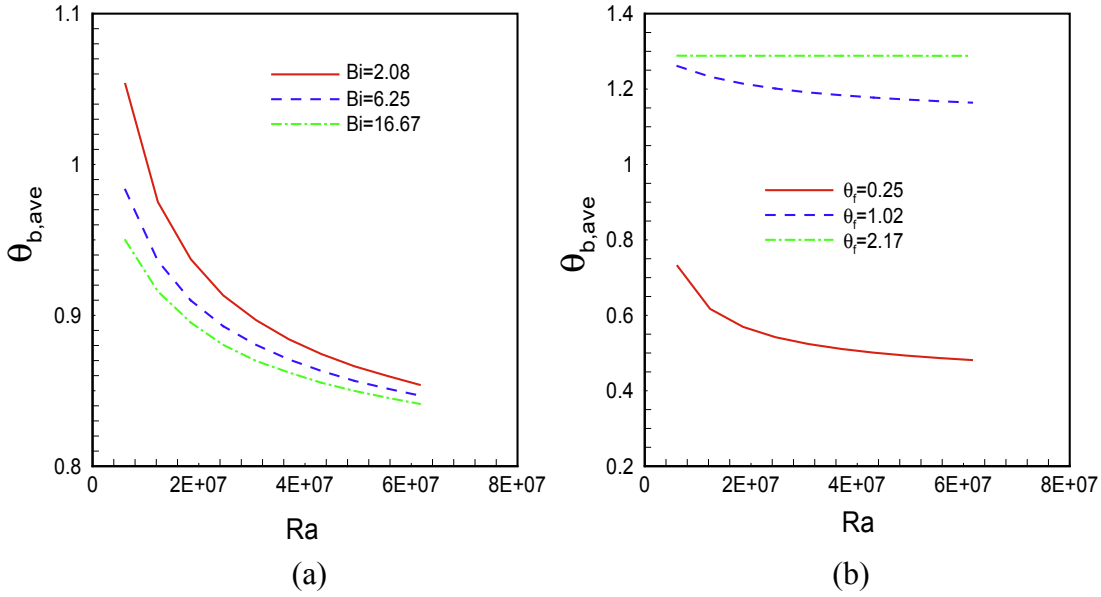

Fig. 9. The average wall temperature ($\theta_{b,ave}$) as a function of Rayleigh number for (a) different Biot numbers; (b): different non-dimensional fusion temperatures (θ_f).

solid formation at the top of the heatsink is much smaller than that of $\gamma = 3$. This is since most regions of the heatsink were at the molten state, and there was a tiny solid region at the bottom of the heatsink at the previous time step of $\tau = 0.4$ (Fig. 10 (i)).

Melting of this region cannot effectively reduce the overheated temperature of the molten liquid in the melted area. It is also worth noticing that no solid area at the top of the heatsink results in lower thermal resistance and facilitates the solid formation. Therefore, a visual comparison between Fig. 10 (i) and (l) confirms that the amount of solid at $\tau = 0.47$ is significantly lower than that of $\tau = 0.4$ for the case of $\gamma = 5$. This is while in the case of $\gamma = 3$, the amount of solid region at $\tau = 0.47$ was slightly higher than that of $\tau = 0.4$. Moreover, the volume of the hot liquid in Fig. 10 (l) is higher than that of Fig. 10 (k).

Fig. 10 (m), (n), and (o) depict the results at a sufficiently long time after the heat pulse turned off. The elapsed non-dimensional time between $\tau = 0.35$ and $\tau = 0.9$ is about 230% of the pulse duration ($\delta\tau = 0.305$). Fig. 10 (m) is almost the same as Fig. 10 (j) indicating the heatsink is approaching to its steady-state condition. Fig. 10 (n) shows the development of a solid region toward the bottom areas of the heatsink. Fig. 10 (o) displays the early stages of solidification at the top of the heatsink. The isotherms are very similar at this time step for all of puls power loads. Indeed, the liquid in the molten region has reached a semi-steady state, and solidification formation slowly advances from the top toward the bottom right corner of the heatsink.

Fig. 11 studies the effect of time-step at melting front for various values of pulse power. Fig. 12 illustrates the effect of pulse power on the melting front at various time-steps. As before, the melt volume fraction of$\phi = 0.5$ was considered as the melting front. Fig. 13(a), (b), and (c) depict the time history of melt volume fraction, the average temperature of the element, and efficiency of the heatsink, respectively. Fig. 11 (a) shows that the melting stopped at $\tau = 0.45$, 0.5 and 0.52 respectively for the pulse power of $\gamma = 1$, 3, and 5 while pulse was turned off at $\tau = 0.35$. This figure reveals that there is a delay between the deactivation of the pulse and suppression of the melting. The increase of the pulse power increases the delay between the turn off time of pulse and suppression of the melting process. Following the results of Fig. 11, the melting front for three-time steps of $\tau = 0.012$, 0.47, and 1.17 are plotted in Figs. 11 and 12.

When the pulse power is low ($\gamma = 1$), Fig. 11(a) shows that the melting advanced toward the top and right of the heatsink. Indeed, the melting advances away from the hot element and slightly toward the top of the heatsink ($\tau = 0.47$). The solidification occurs at the top and advances toward the hot element while the melting front (at the bottom) has shifted away from the hot element, indicating slight degrees of simultaneous melting ($\tau = 0.1.17$). In the case of moderate element power of $\gamma = 3$, melting occurs toward the top wall and slightly toward the right insulated wall ($\tau = 0.47$). There is a minimal layer of solid at the top of the heatsink, which results in a low thermal resistance between the hot molten liquid in the heatsink and the external cooling flow. Considering the solidification ($\tau = 1.17$), the melting front advances from the top toward the bottom.

In the case of $\gamma = 5$, the pulse power is very high, and hence, the natural convection heat transfer is the dominant regime of heat transfer. The bottom is located far from the cold wall, while the top region is subject to a strong natural convection flow of the hot liquid. Hence, the melting front advanced from the bottom as well as toward the top of the heatsink. The solidification commenced from the top with layered shape progress. The solid layer is slightly thinner at the left area of the cold surface as that area is closer to the element and exposed to the natural convection of the hot liquid.

Fig. 10 (a) in agreement with Fig. 10 (a)-(c) shows that the heatsink is at the steady-state before commencing of the heat pulse. Fig. 12 (b) shows that the higher the pulse power, the faster the moving of the melting front away from the heating wall. Fig. 12 (c) depicts that the solidification behavior for all of the pulse powers follows the same trend of behavior. This is since, after the pulse power turned off, the liquid in the molten region gets cold by consuming remaining solid regions at the bottom of the heatsink and interacting with the external cooling power. After a while, the molten region reaches a semi-steady state, and the formation of a solid layer is almost independent of the heat pulse. This is since the heat pulse is already deactivated, and its transient effects are damped in the liquid region. In this situation, the solidification is mainly controlled by external cooling power and the initial element power (Rayleigh number).

Fig. 13 (a) shows the value of melting volume fraction is constant at initial times. On activation of the heat pulse, the *MVF* intensely increases until it reaches a maximum value. As mentioned, the non-dimensional time for the maximum *MVF* is slightly larger than the end time of heat pulse, and it is higher for a higher magnitude of pulse power. After the maximum point, the *MVF* commences decreasing that indicates the occurrence of general solidification in the heatsink. From this figure, it can be seen that the maximum value of *MVF* increases

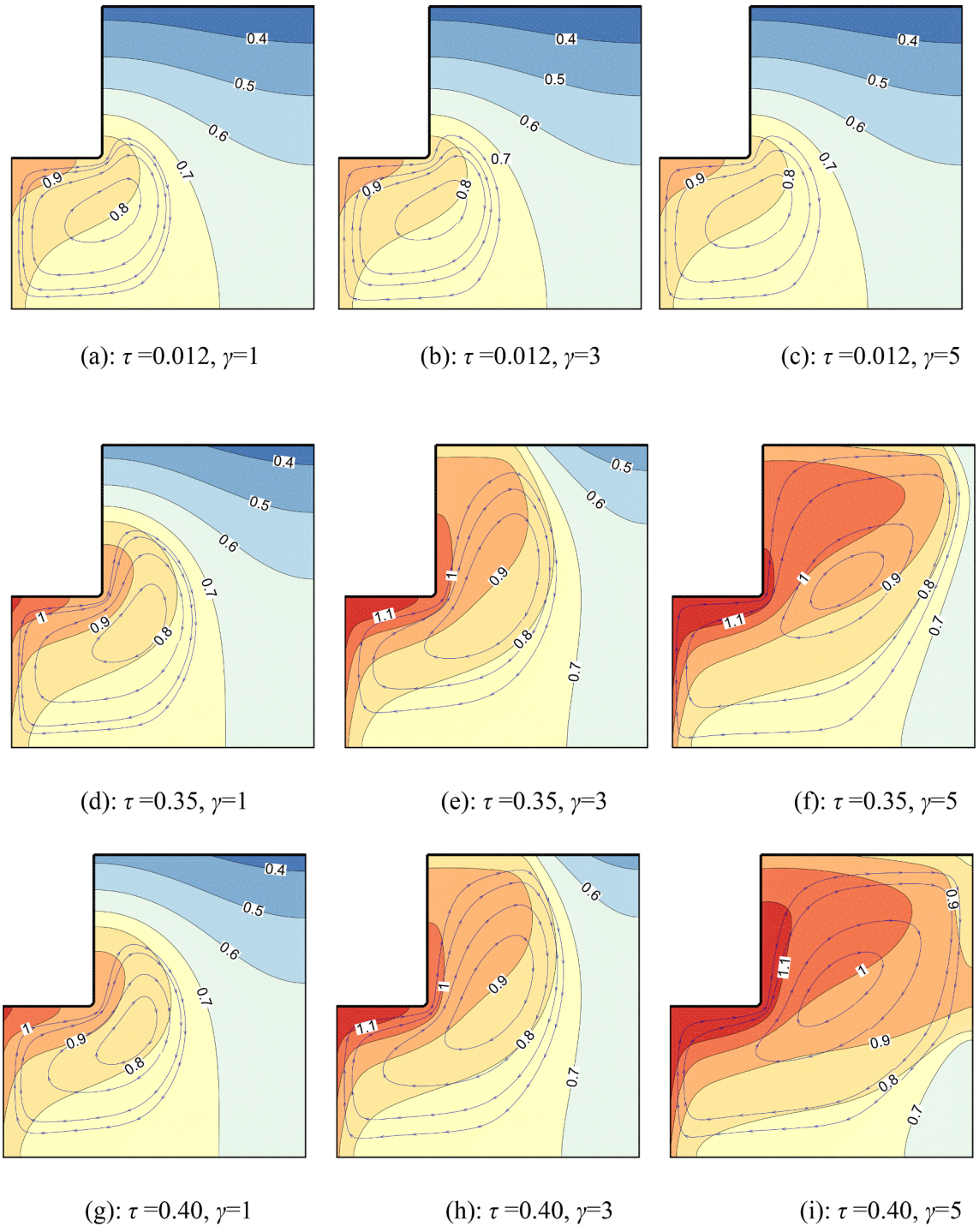

Fig. 10. The effect of heat pulse power (γ) on the isotherms and streamlines at various non-dimensional time steps.

when γ changes from 1 to 5.

Fig. 13 (b) depicts the average dimensionless temperature of the hot element at the left wall. On activation of the heat pulse, $\theta_{b,ave}$ jumps to a high value and remains almost constant during the pulse time. Besides, just after the deactivation of the pulse, the element temperature sharply drops to the initial steady-state value for $\gamma = 1$ and $\gamma = 3$. However, in the case of $\gamma = 5$, it takes some more time to element temperature drops to the initial steady temperature. This is since most regions of the heatsink are in a molten state (as was observed in Fig. 10), and there are minimal solid regions to compensate for the hot liquid and cool down the element. The Fig. 13 (c) displays the efficiency of the heatsink for various values of pulse power. From Fig. 13 (c) it can be concluded that the heatsink efficiency increase when γ goes up. The thermal resistance of the heatsink, which is placed between the hot element and cooling power, is an important parameter, affecting the cooling efficiency of the heatsink.

It should be noted that the fusion temperature of the PCM is higher than the temperature of the external flow, and hence, the temperature difference between the heated wall and the melting front is lower than that of the heated wall and the external flow, if the element was cooled directly by exposing to the external flow. Thus, both the temperature difference and thermal resistance both are barriers for the cooling of the element. However, the convective heat transfer coefficient in the PCM-heatsink, charged by the energy storage capability of the PCM, is the

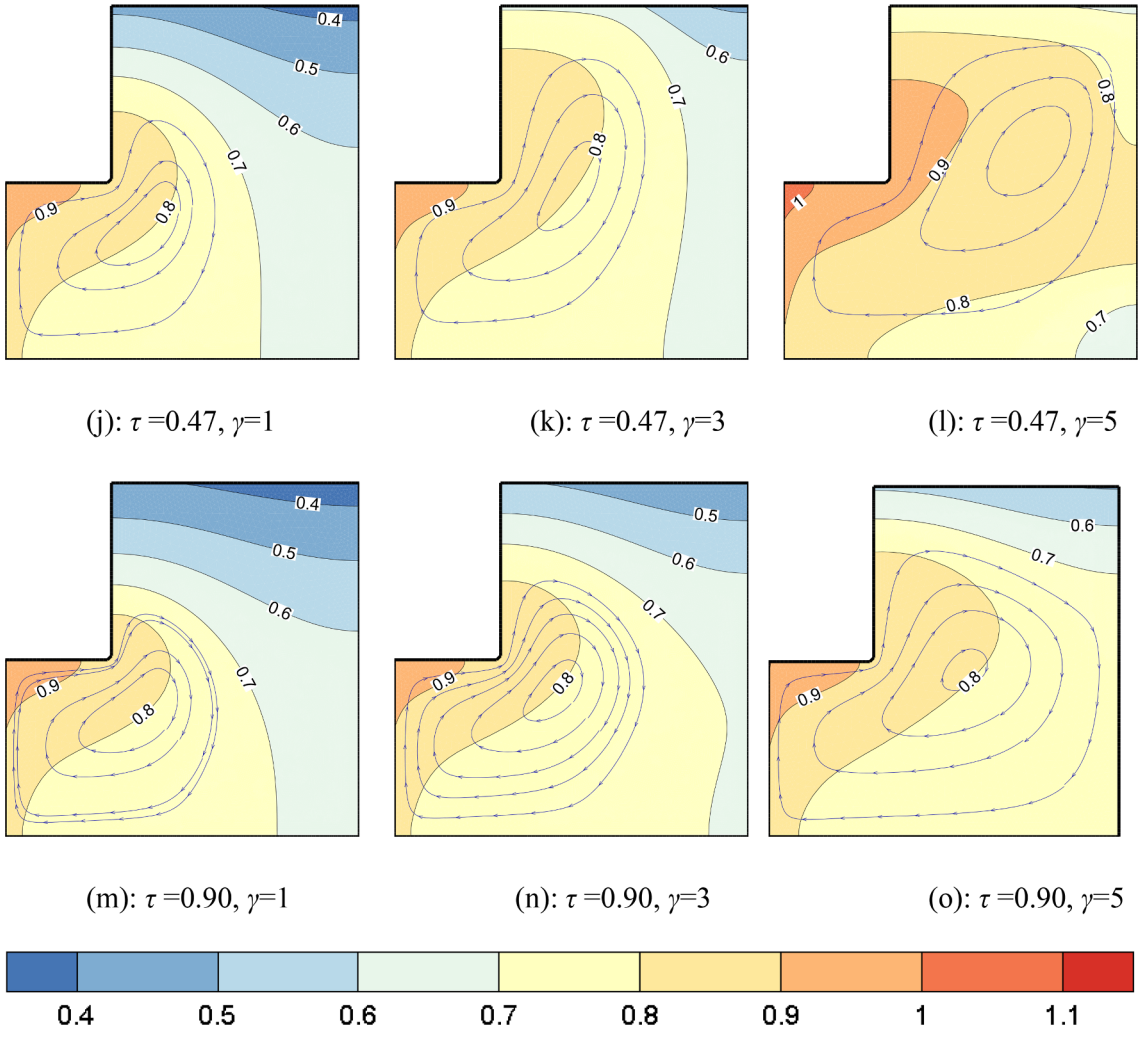

Fig. 10. (*continued*)

key parameter, which can overcome the mentioned barriers.

When the PCM cooling overcomes the direct cooling of the element, the heatsink's efficiency is greater than unity. At the early stages of the heat pulse, the sensible heat of the heatsink plays an important rule and increases the efficiency of the heatsink. This is where a sharp increase in the efficiency of heatsink can be observed when the heat pulse turns on. Then, shortly after the early stage of the activation of the heat pulse, the melting process commences and tries to absorb a significant portion of the produced heat of the element. Some portion of the heat also reaches to the cool wall of the heatsink. When the pulse power is low, the external cooling flow can efficiently absorb the produced heat of the element, and hence, using the heatsink does not provide a notable advantage. However, in the case of moderate or high pulse power, the phase change heat transfer contributes to an extra cooling source. Thus as seen, an increase of pulse power boosts the heatsink efficiency.

The increase of pulse power from moderate power of $\gamma = 3$ to a high power of $\gamma = 5$ improves the heatsink efficiency from 1.75 to 2.5. Indeed, $\gamma = 3$ and $\gamma = 5$ respectively are fourfold and fivefold higher than the steady heat flux. This founding is in agreement with the results of Kandasamy et al. [42], who investigate the thermal management capacity of PCM-finned heatsinks for the cooling of electronic components. They also reported that increasing the steady heating power of the heated surface improves the thermal performance of the heatsink. Based on Fig. 13 (c), the enhancement in the heatsink efficiency by increasing pulse power from 3 to 5 is about 42% (raise of η from 1.75 to 2.25) enhancement of heatsink efficiency. In the experimental study of Hussain et al. [46], a 31% performance enhancement compared to natural air cooling was observed by using nickel foam-paraffin heatsink for thermal management of Li-ion batteries. This performance enhancement qualitatively is in good agreement with the results of the present study. Thus, it can be concluded that the presence of a PCM-metal foam heatsink could efficiently damp the sharp heat loads and protect the heated surface and electronic components.

5. Conclusion

The phase change flow and heat transfer of PCMs embedded in metal foams were studied for heatsink applications. The heatsink was made of an L-shapes channel, in which a part of its left wall was exposed to a pulse heat flux, and an external natural convection flow cooled the top of the heatsink. The enthalpy-porosity approach was employed to model the heat transfer in the heatsink. The governing equations were represented in a non-dimensional form to generalize the study. The finite element method was used to solve the governing equations. Grid adaptation and automatic time step schemes were utilized to improve the accuracy and stability of the solution. The steady-

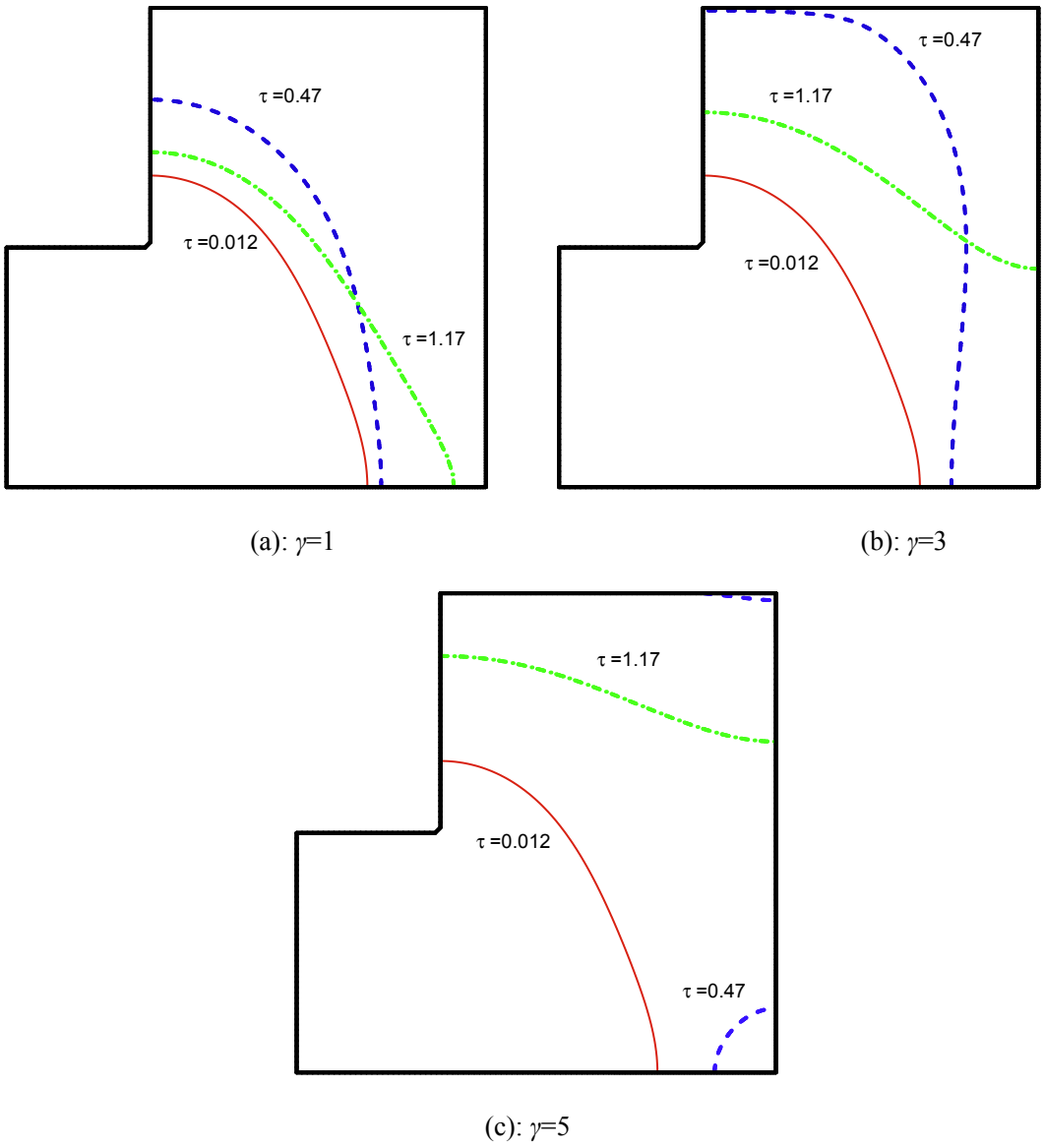

Fig. 11. The behavior of the displacement of the melting front ($\phi = 0.5$) at various times.

state behavior of the phase change heatsink was addressed first. Then, the effect of various heat pulse powers was studied on the melting/solidification behavior of the heatsink. The main outcomes of the present work can be summarized as below:

1. Using the grid adaptation facilitates the accuracy and stability of the solution. An excellent agreement between the results of the present study and the experimental results available in the literature were obtained.
2. Considering a steady-state heatsink with no pulse power. The increase of Rayleigh number and Biot number gradually decreases the average temperature of the element. The increase of Rayleigh number boosts the natural convection flows in the molten region of the heat sink and improves the heat transfer. The increase of Rayleigh number slightly decreases the melting volume fraction in the heatsink. This is since the growth of buoyancy forces shifts the melting front toward the element at the bottom area of the heatsink, but its effect on the melting front is minimal at the top area of the heatsink.
3. During a heat pulse, the melting volume fraction increases gradually. After the deactivation of the heat pulse, the melting volume fraction continues to increase to reach a maximum level, and then, it gradually decreases during the solidification process.
4. During the heat pulse, the temperature of the element elevates sharply and then remains constant. After the heat pulse duration, the temperature of the element again drops toward the steady-state temperature of the heatsink. In the case of low pulse power or moderate pulse power, in which there is a notable amount of residual solid PCM in the heatsink, and hence, the temperature of the element declines sharply after the deactivation of the heat pulse. To the initial steady-state temperature. However, in the case of a high power pulse, most of the heatsink is molten, and hence, there is not enough solid PCM to compensate for the sensible heat of the molten PCM. Consequently, the temperature of the element drops to the

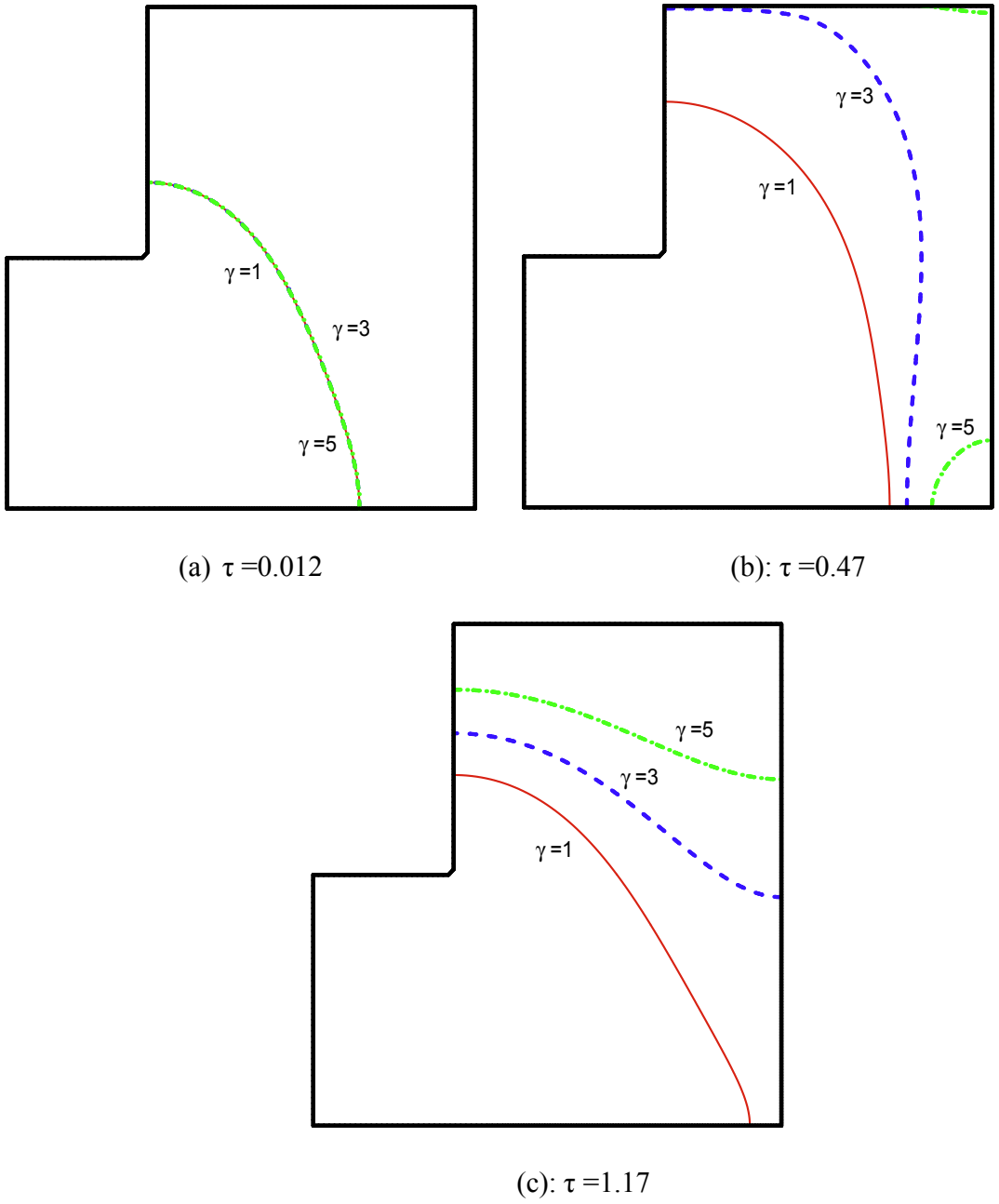

Fig. 12. The behavior of the displacement of the melting front ($\phi = 0.5$) for various pulse power γ.

initial steady-temperature but with some delay.

5. The solidification starts from the top of the heatsink in a stratified form and then extends to the adiabatic right-wall of the enclosure. In some cases, a simultaneous melting and solidification process was observed that tends to shift the location of solid regions from the bottom right corner of the heatsink to the top of the heatsink during the solidification process.
6. The presence of PCM heatsink enhances the heat transfer and reduces the temperature of the element. Generally, utilizing a PCM-metal foam heatsink results in an efficiency higher than unity, which confirms the advantage of the heatsink in thermal management of the heated surface. As the pulse power rises, the efficiency of the heatsink grows gradually during the pulse. The heatsink efficiency raises of 1.75 and 2.5 by the increase of γ from 3 to 5.

The observed heatsink efficiency was higher than unity bout lower than 2.5. Although a heatsink efficiency higher than two can be reasonable to be used, heatsink efficiencies much higher than two are of interest. Hence, a further decrease of PCM-metal foam thermal resistance is of interest. From the phase change behavior of the PCM-metal foam, it is evident that the location of the cooling wall and the hot element can change the behavior of the heatsink. Thus, analysis of the effect of cooling and heating locations such as cooling or heating from the bottom or corner of the heatsink can be subject to future researches.

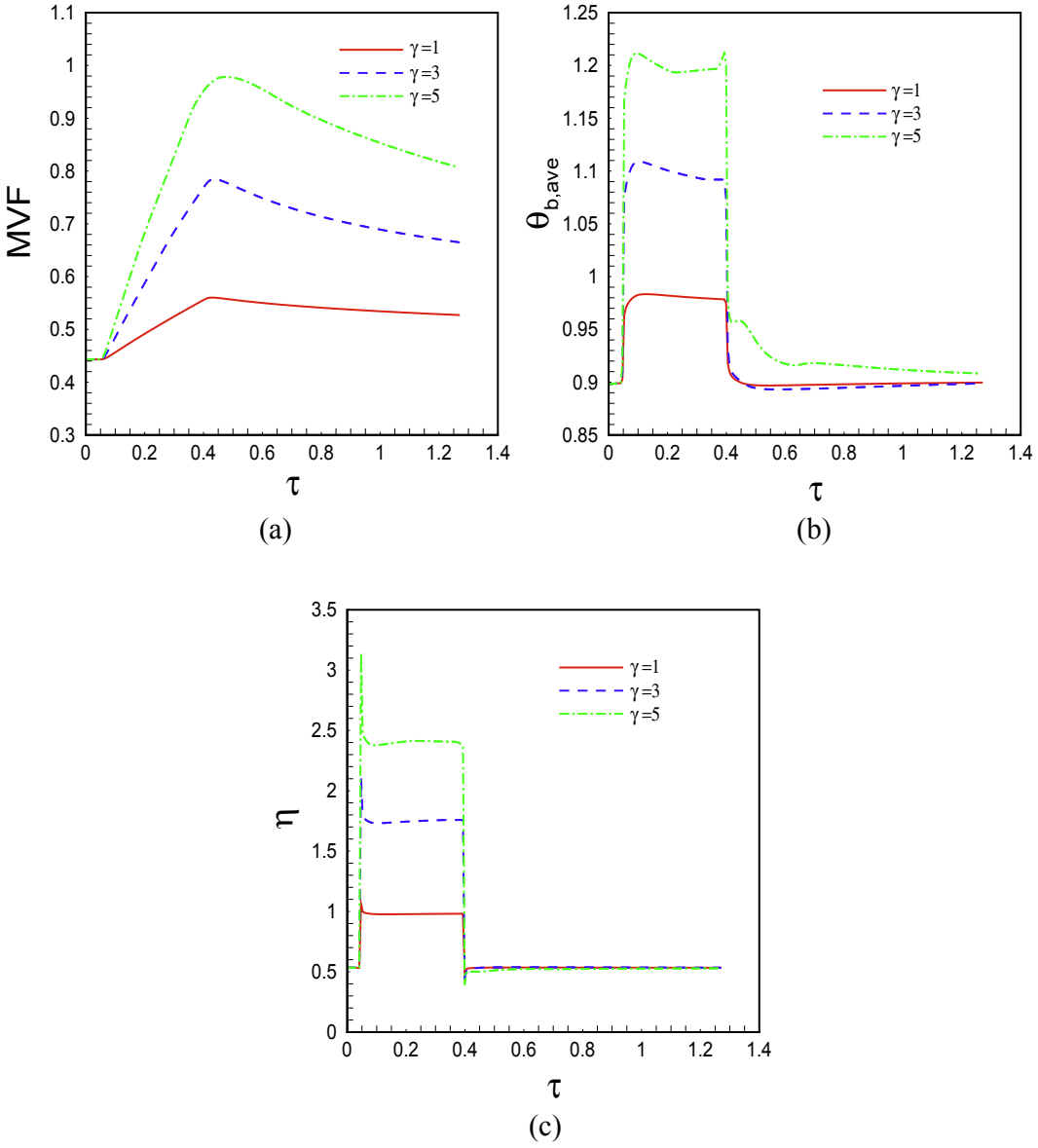

Fig. 13. Time history of the heatsink characteristics for various values of pulse power (γ); (a): normalized melt volume fraction, (b): average element's temperature, and (c): the heatsink efficiency (η).

Declaration of Competing Interest

The authors declared that there is no conflict of interest.

Appendix A. Supplementary material

Supplementary data to this article can be found online at https://doi.org/10.1016/j.applthermaleng.2020.115493.

References

[1] N. Zhang, Y. Yuan, X. Cao, Y. Du, Z. Zhang, Y. Gui, Latent heat thermal energy storage systems with solid–liquid phase change materials: a review, Adv. Eng. Mater. 20 (2018) 1700753.
[2] S.Y. Kee, Y. Munusamy, K.S. Ong, Review of solar water heaters incorporating solid-liquid organic phase change materials as thermal storage, Appl. Therm. Eng. 131 (2018) 455–471.
[3] N.A.C. Sidik, T.H. Kean, H.K. Chow, A. Rajaandra, S. Rahman, J. Kaur, Performance enhancement of cold thermal energy storage system using nanofluid phase change materials: a review, Int. Commun. Heat Mass Transfer 94 (2018) 85–95.
[4] H. Nazir, M. Batool, F.J.B. Osorio, M. Isaza-Ruiz, X. Xu, K. Vignarooban, P. Phelan, A.M. Kannan, Recent developments in phase change materials for energy storage applications: a review, Int. J. Heat Mass Transf. 129 (2019) 491–523.
[5] K. Du, J. Calautit, Z. Wang, Y. Wu, H. Liu, A review of the applications of phase change materials in cooling, heating and power generation in different temperature ranges, Appl. Energy 220 (2018) 242–273.
[6] Y. Lin, Y. Jia, G. Alva, G. Fang, Review on thermal conductivity enhancement, thermal properties and applications of phase change materials in thermal energy storage, Renew. Sustain. Energy Rev. 82 (2018) 2730–2742.
[7] Y. Lin, G. Alva, G. Fang, Review on thermal performances and applications of thermal energy storage systems with inorganic phase change materials, Energy (2018).
[8] N. Bondareva, M. Sheremet, Numerical simulation of natural convection melting in 2D and 3D enclosures, J. Thermal Eng. 5 (2019) 51–61.
[9] N. Bondareva, M. Sheremet, Numerical investigation of the two-dimensional natural convection inside the system based on phase change material with a source of volumetric heat generation, Thermophys. Aeromech. 25 (2018) 525–537.
[10] L. Kumar, B. Manjunath, R. Patel, S. Markandeya, R. Agrawal, A. Agrawal, Y. Kashyap, P. Sarkar, A. Sinha, K. Iyer, Experimental investigations on melting of lead in a cuboid with constant heat flux boundary condition using thermal neutron radiography, Int. J. Therm. Sci. 61 (2012) 15–27.
[11] L. Kumar, B. Manjunath, R. Patel, S. Prabhu, Experimental investigations on melting of lead in a cuboid with constant heat flux boundary condition at two vertical walls using infra-red thermography, Int. J. Heat Mass Transf. 68 (2014) 132–140.
[12] O. Bertrand, B. Binet, H. Combeau, S. Couturier, Y. Delannoy, D. Gobin, M. Lacroix, P. Le Quéré, M. Médale, J. Mencinger, Melting driven by natural convection A comparison exercise: first results, Int. J. Therm. Sci. 38 (1999) 5–26.
[13] N.S. Bondareva, B. Buonomo, O. Manca, M.A. Sheremet, Heat transfer performance

of the finned nano-enhanced phase change material system under the inclination influence, Int. J. Heat Mass Transf. 135 (2019) 1063–1072.
[14] N.S. Bondareva, B. Buonomo, O. Manca, M.A. Sheremet, Heat transfer inside cooling system based on phase change material with alumina nanoparticles, Appl. Therm. Eng. 144 (2018) 972–981.
[15] M. Ghalambaz, A. Doostani, A.J. Chamkha, M.A. Ismael, Melting of nanoparticles-enhanced phase-change materials in an enclosure: effect of hybrid nanoparticles, Int. J. Mech. Sci. 134 (2017) 85–97.
[16] M. Ghalambaz, A. Doostani, E. Izadpanahi, A. Chamkha, Phase-change heat transfer in a cavity heated from below: the effect of utilizing single or hybrid nanoparticles as additives, J. Taiwan Inst. Chem. Eng. 72 (2017) 104–115.
[17] M. Sheikholeslami, R.-U. Haq, A. Shafee, Z. Li, Heat transfer behavior of nanoparticle enhanced PCM solidification through an enclosure with V shaped fins, Int. J. Heat Mass Transf. 130 (2019) 1322–1342.
[18] M. Sheikholeslami, A. Ghasemi, Z. Li, A. Shafee, S. Saleem, Influence of CuO nanoparticles on heat transfer behavior of PCM in solidification process considering radiative source term, Int. J. Heat Mass Transf. 126 (2018) 1252–1264.
[19] M. Sheikholeslami, M. Jafaryar, A. Shafee, Z. Li, Simulation of nanoparticles application for expediting melting of PCM inside a finned enclosure, Physica A 523 (2019) 544–556.
[20] M. Alizadeh, K. Hosseinzadeh, D. Ganji, Investigating the effects of hybrid nanoparticles on solid-liquid phase change process in a Y-shaped fin-assisted LHTESS by means of FEM, J. Mol. Liq. 287 (2019) 110931.
[21] K. Hosseinzadeh, M. Alizadeh, D. Ganji, Solidification process of hybrid nano-enhanced phase change material in a LHTESS with tree-like branching fin in the presence of thermal radiation, J. Mol. Liq. 275 (2019) 909–925.
[22] M. Alizadeh, K. Hosseinzadeh, H. Mehrzadi, D. Ganji, Investigation of LHTESS filled by Hybrid nano-enhanced PCM with Koch snowflake fractal cross section in the presence of thermal radiation, J. Mol. Liq. 273 (2019) 414–424.
[23] A. Doostani, M. Ghalambaz, A.J. Chamkha, MHD natural convection phase-change heat transfer in a cavity: analysis of the magnetic field effect, J. Braz. Soc. Mech. Sci. Eng. 39 (2017) 2831–2846.
[24] M. Ghalambaz, A. Doostanidezfuli, H. Zargartalebi, A.J. Chamkha, MHD phase change heat transfer in an inclined enclosure: effect of a magnetic field and cavity inclination, Numer. Heat Transf. Part A: Appl. 71 (2017) 91–109.
[25] I. Pop, N.C. Roşca, A.V. Roşca, MHD stagnation-point flow and heat transfer of a nanofluid over a stretching/shrinking sheet with melting, convective heat transfer and second-order slip, Int. J. Numer. Meth. Heat Fluid Flow 28 (2018) 2089–2110.
[26] A.J. Chamkha, F. Selimefendigil, MHD mixed convection of nanofluid due to an inner rotating cylinder in a 3D enclosure with a phase change material, Int. J. Numer. Meth. Heat Fluid Flow (2018).
[27] S. Sivasankaran, A. Alsabery, I. Hashim, Internal heat generation effect on transient natural convection in a nanofluid-saturated local thermal non-equilibrium porous inclined cavity, Physica A 509 (2018) 275–293.
[28] M. Ghalambaz, A. Tahmasebi, A. Chamkha, D. Wen, Conjugate local thermal non-equilibrium heat transfer in a cavity filled with a porous medium: Analysis of the element location, Int. J. Heat Mass Transf. 138 (2019) 941–960.
[29] M. Paknezhad, A. Rashidi, T. Yousefi, Z. Saghir, Effect of aluminum-foam heat sink on inclined hot surface temperature in the case of free convection heat transfer, Case Studies Thermal Eng. 10 (2017) 199–206.
[30] M.A. Sheremet, I. Pop, Natural convection in a square porous cavity with sinusoidal temperature distributions on both side walls filled with a nanofluid: Buongiorno's mathematical model, Transp. Porous Media 105 (2014) 411–429.
[31] M.A. Ismael, H.S. Ghalib, Double diffusive natural convection in a partially layered cavity with inner solid conductive body, Sci Iran 25 (2018) 2643–2659.
[32] A.I. Alsabery, T. Tayebi, A.J. Chamkha, I. Hashim, Effect of rotating solid cylinder on entropy generation and convective heat transfer in a wavy porous cavity heated from below, Int. Commun. Heat Mass Transfer 95 (2018) 197–209.
[33] A. Alsabery, A. Chamkha, H. Saleh, I. Hashim, Natural convection flow of a nanofluid in an inclined square enclosure partially filled with a porous medium, Sci. Rep. 7 (2017) 2357.
[34] M.A. Ismael, Double-diffusive mixed convection in a composite porous enclosure with arc-shaped moving wall: tortuosity effect, J. Porous Media 21 (2018).
[35] N.S. Gibanov, M.A. Sheremet, M.A. Ismael, A.J. Chamkha, Mixed convection in a ventilated cavity filled with a triangular porous layer, Transp. Porous Media 120 (2017) 1–21.
[36] X. Xiao, P. Zhang, M. Li, Preparation and thermal characterization of paraffin/metal foam composite phase change material, Appl. Energy 112 (2013) 1357–1366.
[37] H. Zheng, C. Wang, Q. Liu, Z. Tian, X. Fan, Thermal performance of copper foam/paraffin composite phase change material, Energy Convers. Manage. 157 (2018) 372–381.
[38] R. Hossain, S. Mahmud, A. Dutta, I. Pop, Energy storage system based on nanoparticle-enhanced phase change material inside porous medium, Int. J. Therm. Sci. 91 (2015) 49–58.
[39] Z. Li, M. Sheikholeslami, M. Samandari, A. Shafee, Nanofluid unsteady heat transfer in a porous energy storage enclosure in existence of Lorentz forces, Int. J. Heat Mass Transf. 127 (2018) 914–926.
[40] M.S. Al-Jethelah, S.H. Tasnim, S. Mahmud, A. Dutta, Melting of nano-phase change material inside a porous enclosure, Int. J. Heat Mass Transf. 102 (2016) 773–787.
[41] H.M. Ali, A. Arshad, M. Jabbal, P.G. Verdin, Thermal management of electronics devices with PCMs filled pin-fin heat sinks: a comparison, Int. J. Heat Mass Transf. 117 (2018) 1199–1204.
[42] R. Kandasamy, X.-Q. Wang, A.S. Mujumdar, Transient cooling of electronics using phase change material (PCM)-based heat sinks, Appl. Therm. Eng. 28 (2008) 1047–1057.
[43] Z.-Q. Zhu, Y.-K. Huang, N. Hu, Y. Zeng, L.-W. Fan, Transient performance of a PCM-based heat sink with a partially filled metal foam: Effects of the filling height ratio, Appl. Therm. Eng. 128 (2018) 966–972.
[44] W. Alshaer, M. Rady, S. Nada, E.P. Del Barrio, A. Sommier, An experimental investigation of using carbon foam–PCM–MWCNTs composite materials for thermal management of electronic devices under pulsed power modes, Heat Mass Transf. 53 (2017) 569–579.
[45] M. Ghalambaz, J. Zhang, Conjugate solid-liquid phase change heat transfer in heatsink filled with phase change material-metal foam, Int. J. Heat Mass Transf. 146 (2020) 118832.
[46] A. Hussain, C.Y. Tso, C.Y. Chao, Experimental investigation of a passive thermal management system for high-powered lithium ion batteries using nickel foam-paraffin composite, Energy 115 (2016) 209–218.
[47] D.A. Nield, A. Bejan, Convection in Porous Media, 4th ed ed., Springer, 2013.
[48] Y. Xu, M.-J. Li, Z.-J. Zheng, X.-D. Xue, Melting performance enhancement of phase change material by a limited amount of metal foam: Configurational optimization and economic assessment, Appl. Energy 212 (2018) 868–880.
[49] P. Ranut, On the effective thermal conductivity of aluminum metal foams: Review and improvement of the available empirical and analytical models, Appl. Therm. Eng. 101 (2016) 496–524.
[50] A. Bhattacharya, V.V. Calmidi, R.L. Mahajan, Thermophysical properties of high porosity metal foams, Int. J. Heat Mass Transf. 45 (2002) 1017–1031.
[51] J.C. De Los Reyes, S. González Andrade, A combined BDF-semismooth Newton approach for time-dependent Bingham flow, Numer. Methods Partial Differ. Eq. 28 (2012) 834–860.
[52] O. Schenk, K. Gärtner, Solving unsymmetric sparse systems of linear equations with PARDISO, Future Generation Comput. Syst. 20 (2004) 475–487.
[53] P. Wriggers, Nonlinear finite element methods, Springer Science & Business Media, 2008.
[54] F. Verbosio, A. De Coninck, D. Kourounis, O. Schenk, Enhancing the scalability of selected inversion factorization algorithms in genomic prediction, J. Comput. Sci. 22 (2017) 99–108.
[55] C. Beckermann, R. Viskanta, S. Ramadhyani, A numerical study of non-Darcian natural convection in a vertical enclosure filled with a porous medium, Numer. Heat Transfer 10 (1986) 557–570.